

# Supernova 1987A: 3D Mixing and light curves for explosion models based on binary-merger progenitors

V. P. UTROBIN,<sup>1,2,3</sup> A. WONGWATHANARAT,<sup>1</sup> H.-TH. JANKA,<sup>1</sup> E. MÜLLER,<sup>1</sup> T. ERTL,<sup>1</sup> A. MENON,<sup>4</sup> AND A. HEGER<sup>5,6,7,8</sup>

<sup>1</sup>*Max-Planck-Institut für Astrophysik, Karl-Schwarzschild-Str. 1, 85748 Garching, Germany*

<sup>2</sup>*NRC “Kurchatov Institute” – Institute for Theoretical and Experimental Physics, B. Cheremushkinskaya St. 25, 117218 Moscow, Russia*

<sup>3</sup>*Institute of Astronomy, Russian Academy of Sciences, Pyatnitskaya St. 48, 119017 Moscow, Russia*

<sup>4</sup>*Anton Pannekoek Institute of Astronomy, University of Amsterdam, Science Park 904, 1098 XH Amsterdam, Netherlands*

<sup>5</sup>*School of Physics and Astronomy, Monash University, VIC 3800, Australia*

<sup>6</sup>*ARC Centre of Excellence for Gravitational Wave Discovery (OzGrav), Melbourne, Australia*

<sup>7</sup>*ARC Centre of Excellence for Astrophysics in Three Dimensions (ASTRO-3D), Australia*

<sup>8</sup>*Joint Institute for Nuclear Astrophysics, National Superconducting Cyclotron Laboratory, Michigan State University, East Lansing, MI-48824-1321, USA*

(Received XXX; Revised YYY; Accepted ZZZ)

Submitted to ApJ

## ABSTRACT

Six binary-merger progenitors of Supernova 1987A (SN 1987A), whose properties are close to those of the blue supergiant Sanduleak –69°202, are exploded by neutrino heating in three-dimensions (3D), and light-curve calculations are performed in spherical symmetry, starting long after shock breakout. Our results confirm basic findings of previous works using single-star progenitors: (1) 3D neutrino-driven explosions with SN 1987A-like energies synthesize an amount of <sup>56</sup>Ni that is consistent with the radioactive tail of the light curve; (2) hydrodynamic models mix hydrogen inward to minimum velocities below 40 km s<sup>–1</sup> as required by spectral observations of SN 1987A; and (3) for given explosion energy the efficiency of outward radioactive <sup>56</sup>Ni mixing depends mainly on high growth factors of Rayleigh-Taylor instabilities at the (C+O)/He and He/H composition interfaces and a weak interaction of fast plumes with the reverse shock occurring below the He/H interface. All binary-merger models possess presupernova radii consistent with the photometric radius of Sanduleak –69°202 and a structure of the outer layers allowing them to reproduce the observed initial luminosity peak in the first ~7 days. The light curve shape of models that mix about 0.5  $M_{\odot}$  of hydrogen into the helium shell and that exhibit strong outward mixing of <sup>56</sup>Ni with maximum velocities exceeding the 3000 km s<sup>–1</sup> observed for the bulk of ejected <sup>56</sup>Ni is in very good agreement with the dome of the SN 1987A light curve. A comparative analysis of light-curve models of SN 1987A based on 3D neutrino-driven explosions of single-star and binary-merger progenitors shows that only one binary model matches all observational constraints with one exception.

**Keywords:** hydrodynamics — instabilities — nuclear reactions, nucleosynthesis, abundances — shock waves — supernovae: general — supernovae: individual (SN 1987A)

## 1. INTRODUCTION

On February 23, 1987, the outburst of the Type II plateau supernova (SN) 1987A was discovered by Ian Shelton in the Large Magellanic Cloud (LMC) (see Kunkel et al. 1987). This SN became a uniquely peculiar event and one of the most thoroughly studied objects observed from radio wavelengths to gamma-rays. Accurate positional measurement of

the SN showed that its position coincided with that of star 1 from the Sanduleak –69°202 system and a careful examination of the measured *UBVRI* magnitudes indicated that this Sanduleak star was a B3 Ia supergiant (cf. West et al. 1987). These data suggest that the blue supergiant (BSG) star was the progenitor of SN 1987A and permit both single-star and binary evolution scenarios of Sanduleak –69°202.<sup>1</sup>

The fact that SN 1987A was the explosion of the BSG progenitor rather than a red supergiant (RSG) as expected for

Corresponding author: V. P. Utrobin  
utrobin@itep.ru

<sup>1</sup> Henceforward all references to Sanduleak –69°202 only refer to star 1.

ordinary Type IIP SNe, triggered construction of a large variety of evolutionary models to explain the observed properties of Sanduleak –69°202. In the single-star scenario the relative compactness of the BSG progenitor was achieved either by a metal-deficient composition similar to that of the LMC (Truran & Weiss 1987; Hillebrandt et al. 1987; Arnett 1987), a modification of convective mixing through rotation-induced meridional circulation during stellar evolution (Weiss et al. 1988), a restricted semiconvective diffusion and low metallicity (Woosley et al. 1988; Weiss 1989; Langer 1991), or both mass loss and convective mixing (Saio et al. 1988).

All of these possibilities were equally promising until the ESO ground-based New Technology Telescope (Wampler et al. 1990) and the NASA/ESA Hubble Space Telescope (HST, Jakobsen et al. 1991) revealed an intricate triple-ring structure around SN 1987A. The existence of this triple-ring structure imposes additional severe constraints on the evolution of the pre-SN, putting the single-star scenario into doubt and favoring a binary evolution scenario. The evolution of stars in an interacting binary is so rich in possibilities that it permits not only the accretion of a substantial amount of matter from the secondary component onto the pre-SN, but also a complete merger of the two stars. Both abundant accretion of matter from the companion star (Podsiadlowski & Joss 1989) and the merger of the companion star with the primary RSG (Hillebrandt & Meyer 1989; Podsiadlowski et al. 1990, 2007; Menon & Heger 2017; Urushibata et al. 2018) can explain the observed properties of the SN 1987A progenitor.

Podsiadlowski (1992) devised five observational and theoretical tests (the blue color of the progenitor, the ring surrounding it, the chemical anomalies of the progenitor, the characteristics of the SN explosion, and general consistency with the theory of massive stars) and confronted the available evolutionary models for the progenitor of SN 1987A with them. Podsiadlowski concluded that it is most likely that only binary scenario models (accretion and merger models) are able to fit all above constraints.

It is noteworthy that the chemical anomalies of the progenitor included a high nitrogen abundance that was revealed in the circumstellar matter of SN 1987A by an analysis of ultraviolet lines (Fransson et al. 1989) and the overabundance of barium in the ejecta that was estimated by a non-local thermodynamic equilibrium (non-LTE) modeling of optical spectra of SN 1987A (Mazzali et al. 1992). The latter anomaly was revisited and not confirmed when time-dependent effects were taken into account in addition to the non-LTE treatment of spectra (Utrobin & Chugai 2005; Dessart & Hillier 2008), thus softening this constraint.

Over the past quarter of a century, the characteristics of the SN explosion extracted from photometric and spectral observations of SN 1987A have become more and more detailed, especially regarding mixing of radioactive  $^{56}\text{Ni}$  and hydrogen

in the ejected envelope (see Utrobin et al. 2015, for details). Colgan et al. (1994) analyzed the infrared emission lines of [Ni II] and [Fe II] in the nebular phase and found that the bulk of radioactive  $^{56}\text{Ni}$  was moving with a maximum velocity of  $\sim 3000 \text{ km s}^{-1}$ . Additionally, at a higher radial velocity of about  $+3900 \text{ km s}^{-1}$  a unique feature in the infrared emission lines of [Fe II] was found and interpreted as a fast-moving iron clump (Haas et al. 1990). Using the effect of an occultation of this clump by the photosphere on days 29 and 41, Utrobin et al. (1995) estimated its transversal velocity, which together with the radial velocity gives an absolute velocity of  $4700 \text{ km s}^{-1}$ , and identified this high-velocity feature with a fast  $^{56}\text{Ni}$  clump whose luminosity corresponds to a mass of  $\sim 10^{-3} M_{\odot}$ . The analysis of the profiles of hydrogen emission lines in SN 1987A during the nebular phase showed that hydrogen is mixed down into the innermost ejecta to velocities of  $\leq 700 \text{ km s}^{-1}$  (Chugai 1991; Kozma & Fransson 1998; Maguire et al. 2012). The reconstruction of a three-dimensional (3D) view of H $\alpha$  emission (Larsson et al. 2016) and molecular hydrogen (Larsson et al. 2019) revealed that the lowest velocities of hydrogen are observed at  $450 \text{ km s}^{-1}$  and  $400 \text{ km s}^{-1}$ , respectively. Kozma & Fransson (1998) also constrained quantitatively the mass of hydrogen-rich matter which expanded with velocities less than  $2000 \text{ km s}^{-1}$  to about  $2.2 M_{\odot}$ .

Systematic optical and infrared photometric observations of the radioactive tail of SN 1987A carried out by different groups with different instruments permitted them to construct the bolometric light curve and, consequently, to estimate the total mass of ejected  $^{56}\text{Ni}$  – one of the important properties of SN explosions. Dopita et al. (1988) obtained a  $^{56}\text{Ni}$  mass of  $0.085 M_{\odot}$  at the Mount Stromlo and Siding Spring Observatories, Suntzeff et al. (1988) got  $0.071 M_{\odot}$  at the Cerro Tololo Inter-American Observatory, and Catchpole et al. (1989) found  $0.078 M_{\odot}$  at the Sutherland Observatory of the South African Astronomical Observatory. All these masses were obtained with the same distance modulus for the LMC of  $m - M = 18.5 \text{ mag}$ , but different reddening  $E(B - V)$ . Note that Suntzeff & Bouchet (1990) found a range of  $0.055 M_{\odot}$  to  $0.090 M_{\odot}$  for an admissible mass of radioactive  $^{56}\text{Ni}$  using the extreme values of the distance modulus to the LMC ( $18.3 \text{ mag}$  and  $18.6 \text{ mag}$ ) and the reddening ( $0.15 \text{ mag}$  and  $0.20 \text{ mag}$ ). More reliable estimates of the  $^{56}\text{Ni}$  mass with all essential sources of uncertainties taken into account are  $(0.069 \pm 0.003) M_{\odot}$  (Bouchet et al. 1991; McCray 1993) and  $(0.071 \pm 0.003) M_{\odot}$  (Seitenzahl et al. 2014).

One of the central characteristics of an SN explosion is the mass of oxygen in the ejecta. Assuming the most favorable conditions for powering the luminosity of the forbidden oxygen doublet [O I]  $\lambda\lambda 6300, 6364 \text{ \AA}$ , McCray (1993) estimated that a lower limit of the mass of oxygen is about  $0.3 M_{\odot}$ . Li & McCray (1992) calculated the evolution of the intensity and

the profile of the nebular [O I]  $\lambda\lambda 6300, 6364$  Å doublet using a three-zone model with clumps of oxygen and fitted the observational data with an oxygen mass of  $1.3 M_{\odot}$ . Identifying the fluctuations in the profile of the oxygen doublet [O I]  $\lambda\lambda 6300, 6364$  Å with statistical fluctuations of the oxygen clump number, Chugai (1994) found the net oxygen mass to be in the range of  $1.2 M_{\odot}$  to  $1.5 M_{\odot}$ . Chugai et al. (1997) analyzed the 2000 – 8000 Å spectrum of SN 1987A, taken with the HST eight years after the explosion, and concluded that the luminosity of the [O I]  $\lambda\lambda 6300, 6364$  Å doublet is consistent with an oxygen mass in the range of  $1.5 M_{\odot}$ – $2.0 M_{\odot}$ . Applying spectral synthesis non-LTE modeling to the nebular phase spectra, Kozma & Fransson (1998) found that the mass of oxygen gas moving with velocities less than  $2000 \text{ km s}^{-1}$  is about  $1.9 M_{\odot}$ . In turn, Jerkstrand et al. (2015) used a more elaborate spectral synthesis modeling and estimated an oxygen mass as low as  $0.7 M_{\odot}$ , taking the existing uncertainties into account. The mass of oxygen in SN 1987A is thus poorly constrained and ranges from  $0.7 M_{\odot}$  to  $2.0 M_{\odot}$ .

Since SN ejecta expand freely in the nebular phase, when the matter velocity is directly proportional to the radius, it is possible to combine the spectral information and the images along the line of sight to the observer to infer the 3D distribution of the ejecta for the observed emission lines. Kjær et al. (2010) studied the morphology of the ejecta using images and spectra for the emission lines of [Si I]+[Fe II] ( $\lambda 1.64 \mu\text{m}$ ) and He I ( $\lambda 2.058 \mu\text{m}$ ) from the integral field spectroscopy on the Very Large Telescope (VLT) in Chile, which were obtained in October and November 2005. Larsson et al. (2013) presented spectral and imaging observations obtained with the HST between 1994 and 2011 and with the VLT in 2011 at optical and near-infrared wavelengths, particularly in the emission lines of  $H\alpha$  and [Si I]+[Fe II]. Both Kjær et al. and Larsson et al. stated that all these observations show that the ejecta morphology is highly non-spherical. In the case of the [Si I]+[Fe II] and He I lines, the innermost regions of the ejecta are seen and the observed emission represents well the density distribution of these elements. Kjær et al. (2010) approximated the exact 3D shape of the ejecta by a non-spherical distribution and found that an elongated triaxial ellipsoid fits the observations most accurately.

The early hard X-ray and gamma-ray observations of SN 1987A are a powerful tool to test 3D hydrodynamic simulations of neutrino-driven explosions. These observations were carried out with the Roentgen Observatory, the Solar Maximum Mission, the X-ray astronomy satellite *Ginga*, and balloon-borne experiments. Alp et al. (2019) computed the hard X-ray and gamma-ray emission based on 3D neutrino-driven explosion simulations of Wongwathanarat et al. (2013, 2015, 2017) and compared the emergent emission with the corresponding spectra, continuum light curves, and line fluxes of SN 1987A. Jerkstrand et al. (2020) repro-

duced the gamma-ray decay lines and the UVOIR bolometric light curve of SN 1987A up to 600 days by calculating the total gamma-ray deposition for these 3D simulations and found that an ejecta mass around  $14 M_{\odot}$  is favored for an explosion energy of  $1.5 \times 10^{51} \text{ erg}$ .

In our previous papers we studied SN 1987A in the framework of the neutrino-driven explosion mechanism (Utrobín et al. 2015, 2019) using available pre-SN models obtained in the scenario of single-star evolution (Shigeyama & Nomoto 1990; Woosley et al. 1988, 1997; Sukhbold et al. 2016; Utrobín et al. 2019). The corresponding 3D explosion simulations with an approximate, parameterized neutrino engine, when it is tuned to yield the explosion energy observed in SN 1987A, and subsequent hydrodynamic light-curve modeling can explain only some basic observational data. None of the computed models fits all observational constraints, namely, the total  $^{56}\text{Ni}$  mass ejected during the explosion, the amounts of outward  $^{56}\text{Ni}$  mixing and inward hydrogen mixing, the mass of hydrogen mixed to velocities lower than  $2000 \text{ km s}^{-1}$ , and the oxygen mass in the SN ejecta. It is noteworthy that only one model yields a maximum velocity of the bulk of  $^{56}\text{Ni}$  consistent with spectral observations of SN 1987A, and only this model is able to reproduce the dome of the light curve in reasonable agreement with the observed light curve. However, the corresponding progenitor model cannot fulfill the observational requirements of the location of the BSG Sanduleak –69°202 star in the Hertzsprung-Russell diagram (HRD).

This failure in satisfying all basic observational constraints by an adequate progenitor model in the single-star evolution scenario and progress in explaining the formation of the mysterious triple-ring system in the binary-merger evolution scenario (Podsiadlowski et al. 2007; Morris & Podsiadlowski 2009) motivated us to analyze binary-merger progenitor models in the framework of the neutrino-driven explosion mechanism as the next step in our study of SN 1987A. Menon & Heger (2017) presented the results of a systematic study of binary-merger models for the progenitor of SN 1987A, which were evolved until the pre-SN stage. The majority of these models are compact and hot BSG stars, of which six are located in the region of the observed properties of Sanduleak –69°202 in the HRD. Moreover, these evolutionary models reproduce the observed enrichment of helium and nitrogen in the triple-ring nebula, which is characterized by number ratios of  $\text{He}/\text{H} = 0.14 \pm 0.06$  (France et al. 2011),  $\text{N}/\text{C} = 5 \pm 2$  and  $\text{N}/\text{O} = 1.1 \pm 0.4$  (Lundqvist & Fransson 1996). An additional impulse to address the binary-merger progenitors comes from Menon et al. (2019), who computed bolometric light curves using these binary-merger progenitors after exploding them by a piston model in spherical symmetry and applying artificial “boxcar” mixing of chemical species. They obtained a much better agreement of the dome

of the light curves with the observations of SN 1987A than that reported by Utrobin et al. (2019) for the hydrodynamic models based on the single-star progenitor models.

Our present study of 3D explosion simulations of SN 1987A in the framework of neutrino-driven explosions based on binary-merger progenitors provides an opportunity to compare them with those based on the single-star progenitor models in Utrobin et al. (2019). Ono et al. (2020) have recently performed 3D hydrodynamic simulations of mixing in SN 1987A triggering the explosion by injecting energy near the Fe/Si composition interface with parameterized aspherical perturbations of the SN shock to mimic the effect of non-radial instabilities. To reproduce the observed morphology of the ejecta, Ono et al. (2020) investigated two BSG progenitors: one model being the result of a single-star evolution and another model based on a slow merger scenario developed by Urushibata et al. (2018).

Our paper is structured as follows. In Section 2.1 we briefly describe the binary-merger progenitor models and in Section 2.2 we summarize our numerical approach to the 3D simulations of the neutrino-driven explosion and to the hydrodynamic light-curve modeling. Section 3 presents and analyzes the results obtained with the binary-merger pre-SN models and compares them with SN 1987A observations. Section 4 formulates possible requirements for the SN 1987A progenitor that are imposed by the hydrodynamic light-curve modeling. In Section 5 we confront the hydrodynamic models based on the single-star and binary-merger pre-SN models with a set of the available observational constraints of SN 1987A. Finally, in Section 6 we summarize our results.

## 2. MODEL OVERVIEW AND NUMERICAL APPROACH

We consider six pre-SN models obtained in the scenario of binary-merger evolution and use these models as the initial data in our 3D simulations. As in our previous papers, we follow the numerical approach presented in Utrobin et al. (2015). It consists of the three steps: the 3D neutrino-driven explosion simulation until about one day after core collapse, the subsequent mapping of the 3D explosion model to 1D geometry, and the radiation-hydrodynamic modeling of the light curve. We briefly review each step in the corresponding subsection.

### 2.1. Presupernova models

Menon & Heger (2017) carried out a stellar evolution study of binary-merger models for the progenitor of SN 1987A, based on the scenario proposed by Podsiadlowski et al. (1992, 2007). In this scenario a main-sequence secondary star merges with a primary RSG at the end of core helium burning when helium is depleted down to a mass fraction of

1% in the CO rich convective core,<sup>2</sup> surrounded by a helium layer and an extended, expanding hydrogen envelope driving the merger. During the resulting common envelope phase a fraction of the hydrogen-rich secondary mass penetrates the helium core of the primary, whereby an equivalent mass fraction,  $f_c$ , of the He core is dredged up and mixed uniformly in the envelope. Menon & Heger explored an extended parameter space: primary masses of  $15 M_\odot$ ,  $16 M_\odot$ , and  $17 M_\odot$ ; secondary masses of  $2 M_\odot$ ,  $3 M_\odot$ , ...,  $8 M_\odot$ ; and different depths up to which the secondary star penetrates into the He core of the primary star during the common-envelope phase. After the common-envelope phase, the merged star is evolved until just before iron-core collapse. Six of the 84 pre-SN models match the color-luminosity properties of the BSG Sanduleak –69°202 star.

We have investigated these pre-SN models M15-7b, M15-8b, M16-4a, M16-7b, M17-7a, and M17-8a, whose basic properties are listed in Table 1, and whose structure and chemical composition are illustrated by Figures 1 and 2. These binary-merger models having primary stars of  $15 M_\odot$  to  $17 M_\odot$  ( $M_1$ ), secondaries from  $4 M_\odot$  to  $8 M_\odot$  ( $M_2$ ), and a fraction of the He core of the primary that was dredged up of 3.3% to 17.5% evolve to compact blue pre-SN models with masses from  $19.00 M_\odot$  to  $23.81 M_\odot$  ( $M_{\text{pSN}}$ ) and radii of  $31.8 R_\odot$  to  $37.3 R_\odot$  ( $R_{\text{pSN}}$ ).

Because some fraction of the He-shell mass of the helium core<sup>3</sup> of the primary star is dredged up during the merger, all resultant pre-SN models have helium-core masses ( $M_{\text{He}}^{\text{core}}$ ) lower than those of the initial primary stars, while their CO-core masses ( $M_{\text{CO}}^{\text{core}}$ ) remain practically unchanged. As a result, these pre-SN models have much higher mass ratios of the CO core to the helium core in the range of 0.737–0.855 (Table 1) compared to the progenitor models that are evolved in the single-star scenario to a BSG configuration with this mass ratio being in the range of 0.392–0.414 (Utrobin et al. 2019).

The helium-core masses of  $2.90 M_\odot$  to  $4.25 M_\odot$  (Table 1) are much less than the  $6 M_\odot$  suggested for Sanduleak –69°202 as a single star (Saio et al. 1988; Woosley et al. 1988). This should favor stronger outward mixing of radioactive  $^{56}\text{Ni}$  into the hydrogen-rich envelope as observed in SN 1987A, because 3D neutrino-driven explosion simulations with BSG models obtained in the scenario of single-star evolution exhibit  $^{56}\text{Ni}$  mixing whose strength scales very roughly inversely with the helium-core mass (Utrobin et al.

<sup>2</sup> We define the helium-core mass as the mass enclosed by the shell where the mass fraction of hydrogen  $X$  drops below a value of  $X = 0.01$  when moving inward from the surface of a star. The CO-core mass is determined in the same way, but the mass fraction of helium  $Y$  having a value of  $Y = 0.01$ .

<sup>3</sup> Note that Menon & Heger (2017) restrict mixing to be inside the helium shell in their models, quantified by the parameter  $f_{\text{sh}}$  in their work.



**Table 1.** Binary-merger presupernova models for blue supergiants

Model	$M_1$	$M_2$	$f_c$	$M_{\text{CO}}^{\text{core}}$	$M_{\text{He}}^{\text{core}}$	$M_{\text{He}}^{\text{shell}}$	$M_{\text{pSN}}$	$\Delta R_{\text{He}}^{\text{shell}}$	$R_{\text{pSN}}$	$X_{\text{surf}}$	$Y_{\text{surf}}$	$Z_{\text{surf}}$	He/H <sub>surf</sub>	N/C <sub>surf</sub>	N/O <sub>surf</sub>
	( $M_{\odot}$ )		(%)		( $M_{\odot}$ )			( $R_{\odot}$ )				( $10^{-2}$ )			
M15-7b	15	7	17.5	2.48	2.90	0.42	21.06	0.117	37.0	0.6498	0.3447	0.5542	0.134	7.11	1.30
M15-8b	15	8	17.5	2.50	2.95	0.46	22.05	0.143	31.8	0.6529	0.3416	0.5542	0.132	6.34	1.26
M16-4a	16	4	3.3	3.02	4.10	1.08	19.00	0.275	34.9	0.6458	0.3487	0.5536	0.136	7.87	1.40
M16-7b	16	7	16.6	2.81	3.41	0.60	21.98	0.182	37.3	0.6398	0.3547	0.5536	0.140	7.55	1.38
M17-7a	17	7	15.6	3.29	4.25	0.96	22.82	0.182	34.5	0.6540	0.3404	0.5538	0.131	6.44	1.31
M17-8a	17	8	15.6	3.29	4.23	0.94	23.81	0.221	33.4	0.6574	0.3371	0.5539	0.129	6.07	1.27

NOTE—The columns give the name of the pre-SN model; the primary mass,  $M_1$ ; the secondary mass,  $M_2$ ; the fraction of the He core of the primary that was dredged up,  $f_c$ ; the CO-core mass,  $M_{\text{CO}}^{\text{core}}$ ; the He-core mass,  $M_{\text{He}}^{\text{core}}$ ; the He-shell mass,  $M_{\text{He}}^{\text{shell}}$ ; the pre-SN mass,  $M_{\text{pSN}}$ ; the width of the He shell,  $\Delta R_{\text{He}}^{\text{shell}}$ ; the pre-SN radius,  $R_{\text{pSN}}$ ; the mass fractions of hydrogen,  $X_{\text{surf}}$ , helium,  $Y_{\text{surf}}$ , heavy elements,  $Z_{\text{surf}}$ , the number ratios of helium to hydrogen, He/H<sub>surf</sub>, nitrogen to carbon, N/C<sub>surf</sub>, and nitrogen to oxygen, N/O<sub>surf</sub>, in the hydrogen-rich envelope at the stage of core collapse.

2019). In turn, the unchanged CO-core masses of  $2.48 M_{\odot}$  to  $3.29 M_{\odot}$  inherited from moderately massive primary stars (Table 1) should allow for a better match of the oxygen mass observed in the SN 1987A ejecta.

The pre-SN models have different helium core masses in a relatively narrow range of  $2.90 M_{\odot}$  to  $4.25 M_{\odot}$  (Table 1, Figures 1(a) and (c)), and high ratios of the CO-core mass to the helium-core mass in the range of 0.737–0.855 (Table 1). These facts imply that the structure of the helium core in these models should be quite different from that in the single-star progenitor models. Indeed, the difference becomes evident from an inspection of Figure 1(d), Figure 1(d) in Utrobin et al. (2015), and Figure 1(d) in Utrobin et al. (2019), and we extend our previous work on analyzing the sensitivity of the amount of outward  $^{56}\text{Ni}$  mixing and inward hydrogen mixing to the structure of the helium core and the He/H composition interface.

The initial, on the main sequence, chemical composition of the primary and secondary stars was taken to be representative of the subsolar metallicity of the LMC. To produce such a metallicity, the present-day solar chemical composition with the mass fractions of hydrogen  $X = 0.7381$ , helium  $Y = 0.2485$ , and metals  $Z = 0.0134$  (Asplund et al. 2009) was scaled by reducing the total abundance of heavy elements by about a factor of 2.5 compared to solar. The chemical composition of the LMC becomes  $X = 0.739$ ,  $Y = 0.255$ , and  $Z = 0.0055$ . During the binary-merger evolution, the chemical composition at the surface of the primary is enriched with helium and the ashes of CNO-burning dredged up from the core to the envelope, yielding high number ratios of helium to hydrogen (0.129–0.140), nitrogen to carbon (6.07–7.87), and nitrogen to oxygen (1.26–1.40) (Table 1), which are comparable with the observational data (France et al. 2011; Lundqvist & Fransson 1996). The resultant chemical compositions of the pre-SN models M15-7b, M16-4a, M17-7a, M15-8b, M16-7b, and M17-8a are shown in Figure 2.

## 2.2. Numerical methods

For completeness, we briefly summarize the numerical methods used in our work in the following, basically repeating the information that we already provided in our previous paper on SN 1987A (Utrobin et al. 2019), because our methodical approach here is identical with the one applied there.

Our 3D neutrino-driven explosion simulations begin shortly after the stellar core has collapsed and a newly formed SN shock wave has propagated to a mass coordinate of approximately  $1.25 M_{\odot}$  inside the iron core. The evolution during core collapse and core bounce until about 10 ms after bounce is computed in spherical symmetry (because non-radial hydrodynamic instabilities are not expected to grow until this time). These 1D post-bounce data are then mapped onto a 3D grid. The subsequent 3D calculations are carried out with the time-explicit finite-volume Eulerian multi-fluid hydrodynamics code PROMETHEUS (Fryxell et al. 1991; Müller et al. 1991a,b). Details of the physics modules implemented into the PROMETHEUS code and our numerical setup have been described in Wongwathanarat et al. (2013) for neutrino-driven explosion simulations and in Wongwathanarat et al. (2015) for simulations of the late-time evolution from approximately 1.3 s after core bounce onward. Nevertheless, we briefly summarize the input physics and numerical methods employed by the PROMETHEUS code as follows.

The PROMETHEUS code uses a dimensionally split version of the piecewise parabolic method (Colella & Woodward 1984) to solve the multidimensional hydrodynamic equations. A fast and efficient Riemann solver for real gases (Colella & Glaz 1985) is used to compute numerical fluxes at cell boundaries. Inside grid cells, where a strong shock wave is present, we recompute the inter-cell fluxes using an approximate Riemann solver (Liou 1996) to prevent numerical artifacts known as the odd-even decoupling (Quirk 1994). The Yin-Yang overlapping grid (Kageyama & Sato 2004), implemented into PROMETHEUS as in Wongwathanarat

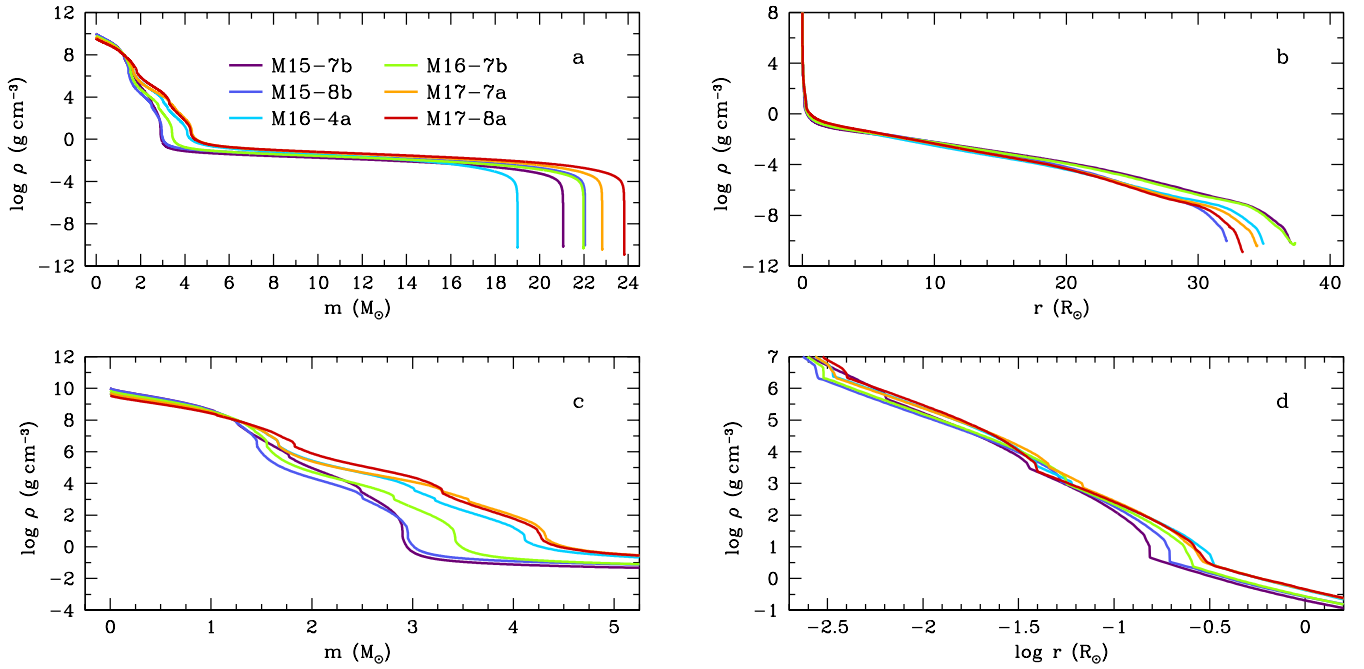


**Figure 1.** Density distributions as functions of interior mass for the whole star (a) and the inner region of  $5 M_{\odot}$  (c), and as functions of radius for the whole star (b) and the inner region of  $1 R_{\odot}$  (d) in the pre-SN models M15-7b, M15-8b, M16-4a, M16-7b, M17-7a, and M17-8a given in Table 1.

et al. (2010), is employed for efficient spatial discretization of the computational domain. Newtonian self-gravity is taken into account by solving Poisson’s equation in its integral form, using an expansion into spherical harmonics (Müller & Steinmetz 1995). In addition, a general relativistic correction of the monopole term of the gravitational potential is applied during the explosion simulations following Scheck et al. (2006) and Arcones et al. (2007).

To model the explosive nucleosynthesis approximately, a small  $\alpha$ -chain reaction network, similar to the network described in Kifonidis et al. (2003), is solved. In order to unambiguously determine the inward mixing of hydrogen, free protons, which are produced when neutrino-heated matter freezes out from nuclear statistical equilibrium, are distinguished from hydrogen originating from the hydrogen-rich stellar envelope by tagging them as different species in our multicomponent treatment of the stellar plasma.

The revival of the stalled SN shock and the explosion are triggered by imposing a suitable value of the neutrino luminosities at an inner radial grid boundary located at an enclosed mass of  $1.1 M_{\odot}$ , well inside the neutrinosphere. Outside this boundary, which shrinks with time to mimic the contraction of the proto-neutron star, we model neutrino-matter interactions by solving the neutrino radiation transport equation in a “ray-by-ray” manner and in the gray approximation as described in Scheck et al. (2006). The explosion energy of the model is determined by the imposed isotropic neutrino luminosity, whose temporal evolution we prescribe as well, and by the accretion luminosity that results from the progenitor-

dependent mass accretion rate and the gravitational potential of the contracting neutron star.

Our 3D calculations are terminated at approximately one day after the onset of the explosion, i.e. long after the SN shock has swept through the entire progenitor star and has broken out from the stellar surface (about 1–2 hours after core bounce; see Table 2). We use a two-step procedure of mapping at two different mapping epochs: an early-time mapping epoch well prior to the phase of shock breakout and a late-time mapping epoch when the 3D explosion simulations are terminated. The early-time mapping moment is chosen to adequately treat the shock breakout, because this breakout is a complex process including the effects of both hydrodynamics and radiative transfer and has to be modeled with a radiation hydrodynamics code. To this end, we compute angle-averaged profiles of hydrodynamic quantities and chemical abundances of the 3D flow and interpolate these profiles onto the Lagrangian (mass) grid used in the 1D simulations. The resulting data are the initial conditions for the hydrodynamic modeling of the SN outburst. The further time evolution of the SN outburst is modeled in one dimension. At the early-time mapping epoch the hydrodynamic flow is far from homologous expansion. This implies that outward mixing of radioactive  $^{56}\text{Ni}$  and inward mixing of hydrogen-rich matter in the ejecta will continue until complete homology is reached. To capture this mixing, we map angle-averaged profiles of chemical abundances of the 3D flow onto the Lagrangian grid at the terminal time of the 3D simulations, when the ejecta expand almost homologously.

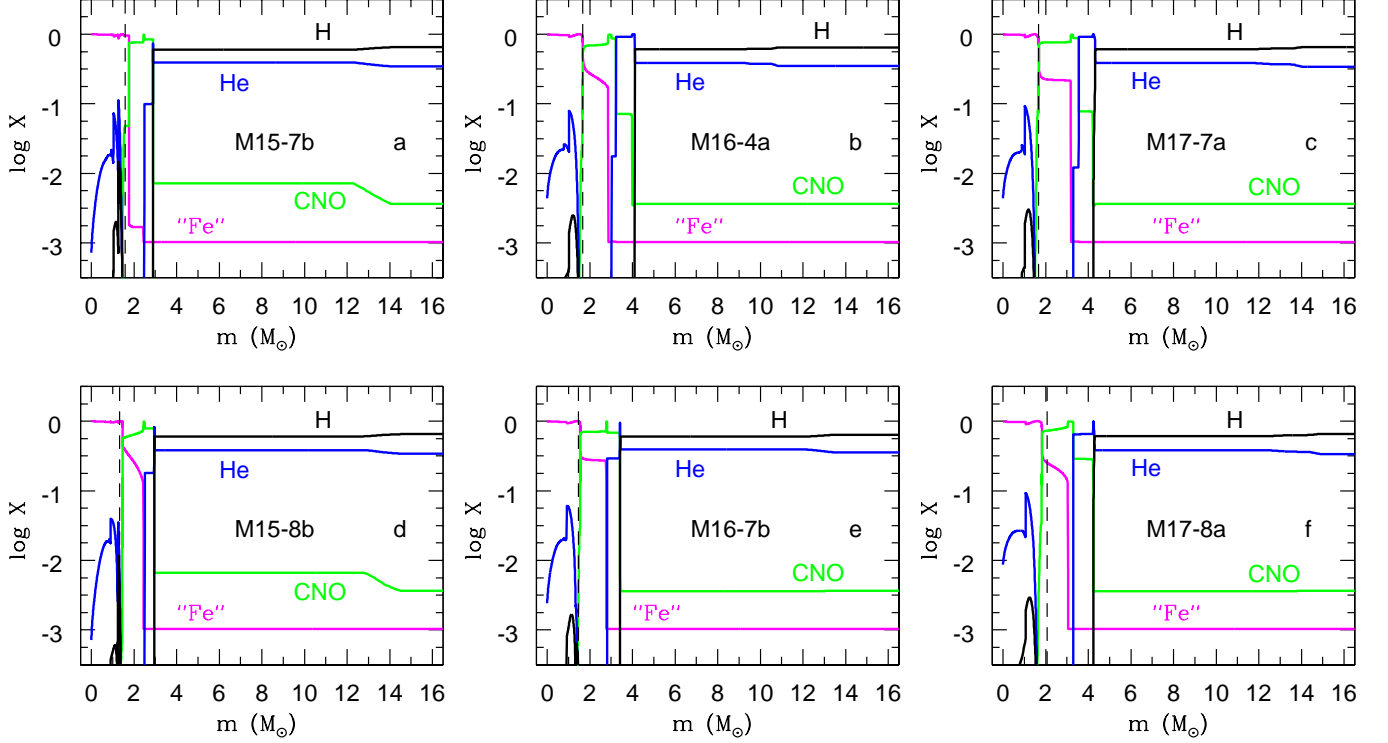


**Figure 2.** Mass fractions of hydrogen (black line), helium (blue line), CNO group elements (green line), and iron group elements (magenta line) in the pre-SN models M15-7b (a), M16-4a (b), M17-7a (c), M15-8b (d), M16-7b (e), and M17-8a (f) (Table 1). The vertical black dashed lines mark the location of the final mass cut in the corresponding six reference 3D explosion models M15-7b-3, M15-8b-1, M16-4a-1, M16-7b-2, M17-7a-2, and M17-8a-4 (Table 2).

After mapping the 3D simulations data to a 1D grid, the evolution of the SN outburst is modeled with the time-implicit Lagrangian radiation hydrodynamics code CRAB (Utrobin 2004, 2007). It integrates the set of spherically symmetric hydrodynamic equations including self-gravity and a radiation transfer equation in the gray approximation (e.g., Mihalas & Mihalas 1984). The whole SN ejecta can be divided into two regions: the inner optically thick core and the outer semitransparent and optically thin layers. In the inner opaque core, the radiation transport is reduced to the diffusion of equilibrium radiation in the approximation of radiative heat conduction, and the assumption of LTE is valid. In the semitransparent and transparent layers, the time-dependent radiative transfer equation, written in a comoving frame of reference to an accuracy of order  $v/c$  ( $v$  is the fluid velocity, and  $c$  is the speed of light), is solved as a system of equations for the zeroth and first angular moments of the nonequilibrium radiation intensity. To close this system of two moment equations, a variable Eddington factor is directly calculated with the scattering terms included explicitly in the source function. The total set of equations is discretized spatially using the method of lines (e.g., Hairer et al. 1993; Hairer & Wanner 1996). The resultant system of ordinary differential equations is integrated by the implicit

method of Gear (1971) with an automatic choice of both the time integration step and the order of accuracy of the method.

The energy deposition of gamma-rays from the decay chain  $^{56}\text{Ni} \rightarrow ^{56}\text{Co} \rightarrow ^{56}\text{Fe}$  is determined by solving the gamma-ray transport, while the corresponding positrons are assumed to deposit their kinetic energy locally. The ionization balance for an ideal gas in a nonequilibrium radiation field and under the influence of non-thermal processes provides the level populations to calculate the equation of state, the mean opacities, and the thermal emission coefficient. It includes the elements H, He, C, N, O, Ne, Na, Mg, Si, S, Ar, Ca, Fe, and the negative hydrogen ion  $\text{H}^-$ . In addition, in expanding SN ejecta with a velocity gradient, the contribution of spectral lines to the opacity is evaluated by the generalized formula of Castor et al. (1975). We refer to Utrobin et al. (2015) and references therein for more details of the numerical setup.

### 3. RESULTS

We carried out fourteen 3D neutrino-driven explosion simulations with the six binary-merger pre-SN models M15-7b, M15-8b, M16-4a, M16-7b, M17-7a, and M17-8a (Table 1) as initial data. Table 2 lists basic properties of these 3D hydrodynamic models that were extracted at the end of the simulations. We define the explosion energy,  $E_{\text{exp}}$ , as the sum of the total (i.e., internal plus kinetic plus gravi-

**Table 2.** Basic properties of the 3D explosion models

Model	$M_{\text{NS}}$	$M_{\text{ej}}$	$E_{\text{exp}}$	$M_{\text{Ni}}^{\text{min}}$	$M_{\text{Ni}}^{\text{max}}$	$M_{\text{Ni}}^{\text{i}}$	$M_{\text{Ni}}^{\text{f}}$	$v_{\text{Ni}}^{\text{bulk}}$	$\langle v \rangle_{\text{Ni}}^{\text{tail}}$	$v_{\text{H}}^{\text{mix}}$	$\delta M_{\text{H}}^{\text{mix}}$	$\Delta M_{\text{H}}^{2000}$	$M_{\text{O}}$	$t_{\text{map}}$	$t_{\text{SB}}$
	( $M_{\odot}$ )	( $M_{\odot}$ )	(B)		( $10^{-2} M_{\odot}$ )				( $\text{km s}^{-1}$ )			( $M_{\odot}$ )		( $10^3 \text{ s}$ )	
M15-7b-1	1.57	19.48	1.404	3.86	14.23	7.37	7.34	3018	3185	29	0.48	3.21	0.83	86.39	5.32
M15-7b-2	1.55	19.49	1.428	4.91	14.96	7.34	7.31	3406	3607	28	0.48	3.07	0.84	86.40	5.34
M15-7b-3	1.58	19.46	1.432	4.79	14.64	7.31	7.28	2980	3193	29	0.49	3.10	0.83	86.39	5.20
M15-7b-4	1.49	19.56	1.780	4.88	17.08	7.33	7.31	3344	3553	28	0.50	2.20	0.86	86.40	4.74
M15-8b-1	1.32	20.73	1.567	2.67	12.07	7.42	7.40	1829	1949	27	0.52	3.14	0.96	86.41	4.54
M15-8b-2	1.38	20.66	1.116	2.32	8.63	7.37	7.32	1439	1535	27	0.44	5.50	0.96	86.40	5.29
M16-4a-1	1.66	17.34	1.562	4.84	14.99	7.50	7.41	2436	2732	29	0.55	2.13	0.97	86.41	4.26
M16-4a-2	1.87	17.13	1.068	3.79	10.25	7.74	7.28	2237	2445	32	0.43	3.55	0.88	86.39	5.02
M16-7b-1	1.53	20.44	1.168	2.83	10.00	7.35	7.26	1639	1759	29	0.51	5.01	1.13	86.41	5.87
M16-7b-2	1.46	20.51	1.412	2.97	11.47	7.39	7.34	1714	1838	28	0.56	3.80	1.16	86.40	5.35
M17-7a-1	1.68	21.13	1.516	4.28	13.91	7.48	7.36	1807	1910	30	0.59	3.75	1.28	86.42	4.65
M17-7a-2	1.67	21.14	1.559	4.60	14.10	7.52	7.41	1713	1888	29	0.56	3.60	1.29	86.41	4.55
M17-8a-3	2.22	21.58	1.075	7.68	11.67	7.69	7.22	2461	2653	32	0.51	6.41	0.90	86.39	5.27
M17-8a-4	2.06	21.75	1.216	6.52	12.67	7.51	7.25	2411	2520	32	0.53	5.62	1.02	86.41	5.02

NOTE—The 3D explosion models are based on the corresponding pre-SN models of Table 1.  $M_{\text{NS}}$  is the baryonic mass of the neutron star at the end of the 3D simulations;  $M_{\text{ej}}$  the ejecta mass;  $E_{\text{exp}}$  the explosion energy;  $M_{\text{Ni}}^{\text{min}}$  the mass of radioactive  $^{56}\text{Ni}$  produced directly by our  $\alpha$ -chain reaction network;  $M_{\text{Ni}}^{\text{max}}$  the aggregate mass of directly produced  $^{56}\text{Ni}$  and tracer nucleus;  $M_{\text{Ni}}^{\text{i}}$  the initial  $^{56}\text{Ni}$  mass at the onset of the light curve modeling;  $M_{\text{Ni}}^{\text{f}}$  the  $^{56}\text{Ni}$  mass ejected at day 150;  $v_{\text{Ni}}^{\text{bulk}}$  the maximum velocity of the bulk mass of  $^{56}\text{Ni}$ ;  $\langle v \rangle_{\text{Ni}}^{\text{tail}}$  the mean velocity of the fast moving  $^{56}\text{Ni}$  tail;  $v_{\text{H}}^{\text{mix}}$  the minimum velocity of hydrogen mixed into the He shell, specified at the level where the mass fraction of hydrogen  $X$  drops to a value of  $X = 0.01$ ;  $\delta M_{\text{H}}^{\text{mix}}$  the mass of hydrogen mixed into the He shell;  $\Delta M_{\text{H}}^{2000}$  the mass of hydrogen confined to the inner layers ejected with velocities less than  $2000 \text{ km s}^{-1}$ ; and  $M_{\text{O}}$  the total mass of oxygen in the ejecta.  $t_{\text{map}}$  is the time at which the 3D simulations are mapped to a spherically symmetric grid.  $t_{\text{SB}}$  is the epoch of shock breakout in the 1D simulations.

tational) energy of all grid cells at the early-time mapping epoch. Throughout this paper, we employ the energy unit 1 bethe =  $1 \text{ B} = 10^{51} \text{ erg}$ . To characterize mixing of radioactive  $^{56}\text{Ni}$  in radial velocity space, we divide the  $^{56}\text{Ni}$ -rich ejecta into two components: a slow-moving bulk of  $^{56}\text{Ni}$  containing 99% of the total  $^{56}\text{Ni}$  mass (except for places in which it is specially defined), and a fast-moving  $^{56}\text{Ni}$  tail containing the remaining 1%. This division is motivated by the observational evidence for a fast  $^{56}\text{Ni}$  clump of  $\sim 10^{-3} M_{\odot}$  in SN 1987A (Utrobin et al. 1995).

### 3.1. Production of $^{56}\text{Ni}$ in neutrino-driven simulations

Along with the explosion energy, the total amount of radioactive  $^{56}\text{Ni}$  plays a crucial role in powering the dome-like maximum of the observed light curve of SN 1987A. To study the production of  $^{56}\text{Ni}$  during our 3D SN simulations, we solved a small  $\alpha$ -chain reaction network from helium through  $^{56}\text{Ni}$  and are therefore unable to determine the mass fraction of  $^{56}\text{Ni}$  in neutron-rich matter very accurately. The so-called “tracer” nucleus collects iron-group and trans-iron species that are formed in neutron-rich ( $Y_e < 0.49$ ) ejecta (Kifonidis et al. 2003; Wongwathanarat et al. 2013). A pos-

sible overall production of radioactive  $^{56}\text{Ni}$  falls in between the minimum and maximum values: the mass of  $^{56}\text{Ni}$  produced directly by our  $\alpha$ -chain reaction network,  $M_{\text{Ni}}^{\text{min}}$ , and the aggregate mass of directly produced  $^{56}\text{Ni}$  plus tracer nucleus,  $M_{\text{Ni}}^{\text{max}}$ . 3D neutrino-driven explosion simulations of SN 1987A based on the single-star pre-SNe showed that the  $^{56}\text{Ni}$  production is proportional to the explosion energy with the correlation being valid for both the minimum and maximum values (Utrobin et al. 2015, 2019). It should be noted that in those simulations the values of the explosion energy are clearly different to guarantee this correlation. In turn, all of the 3D neutrino-driven explosion simulations based on the binary-merger pre-SNe confirm the results of Utrobin et al. (2015, 2019) for the single-star pre-SNe except for two pairs of hydrodynamic models (M15-7b-2, M15-7b-3) and (M17-8a-3, M17-8a-4) (Table 2). These exceptions are worth to be discussed in the context of uncertainties of the production of  $^{56}\text{Ni}$  (see Ertl et al. 2020, for details) and properties of the explosion mechanism itself.

Models M15-7b-2 and M15-7b-3 which explode with nearly the same energies of 1.428 B and 1.432 B, respectively, produce nearly the same mass of radioactive  $^{56}\text{Ni}$  plus



neutron-rich tracer nucleus, but slightly violate the above  $^{56}\text{Ni}$  production–explosion energy correlation for both the minimum and maximum amounts of  $^{56}\text{Ni}$  (Table 2). This small difference in the  $^{56}\text{Ni}$  production between models M15-7b-2 and M15-7b-3 can arise from a number of reasons. First, Ertl et al. (2020) argued that the mass of nucleosynthesis products that scales with the explosion energy should include all other elements that are present in neutrino-heated ejecta (like  $\alpha$ -particles, free neutrons, and protons) in addition to radioactive  $^{56}\text{Ni}$  and the tracer nucleus. In other words, we have to consider at least the maximum amount of  $^{56}\text{Ni}$  as a measure of the explosion energy rather than the minimum amount, but depending on the entropy of the ejecta significant amounts of alpha particles and free nucleons may also be ejected. Second, such a small scattering in the  $^{56}\text{Ni}$  production can result from a simple stochasticity of 3D hydrodynamic instabilities and turbulence. Third, it seems that model M15-7b-3 makes more fallback and therefore some of the initially expelled material in the neutrino-heated ejecta falls back, more than in model M15-7b-2, because the mass of the neutron star in model M15-7b-3 is larger than in model M15-7b-2. Note that in model M15-7b-3 the maximum velocity of the bulk mass of  $^{56}\text{Ni}$  of  $2980 \text{ km s}^{-1}$  is lower than the value of  $3406 \text{ km s}^{-1}$  in model M15-7b-2, favoring more fallback of iron-group material in model M15-7b-3. So, we may state that the violation of the  $^{56}\text{Ni}$  production–explosion energy correlation in the case of models M15-7b-2 and M15-7b-3 is a subtle effect that depends on small differences in details of the explosion dynamics.

Models M17-8a-3 and M17-8a-4, in turn, show perfect scaling of the mass of directly produced  $^{56}\text{Ni}$  plus tracer nucleus,  $M_{\text{Ni}}^{\text{max}}$ , with the explosion energy (Table 2), which is in agreement with the  $^{56}\text{Ni}$  production–explosion energy correlation. Another fact consistent with this correlation is the mass of the neutron star in model M17-8a-4, which is lower than in model M17-8a-3 because more neutrino-heated matter is ejected and contributes to the mass of directly produced  $^{56}\text{Ni}$  plus tracer nucleus instead of being added to the neutron star. The inverse correlation of the explosion energy with the mass of directly produced  $^{56}\text{Ni}$ , is explained by the fact that model M17-8a-4 produces more tracer matter than model M17-8a-3 at the expense of the directly produced  $^{56}\text{Ni}$ .

### 3.2. Mixing in 3D explosion simulations

The development of neutrino-driven explosions after core bounce and the general picture of concomitant turbulent mixing in 3D simulations are described and studied in detail by Wongwathanarat et al. (2015). Here we only recall that after the SN shock wave is launched by the delayed neutrino-driven mechanism, supported by convective overturn and large-scale aspherical shock oscillations caused by the standing accretion shock instability (SASI), the further evolution

of the explosion depends strongly on the density profile of the progenitor. The shock decelerates when it encounters a density profile that falls off less steeply than  $\rho \sim r^{-3}$ , and it accelerates for density profiles that are steeper (Sedov 1959). At the locations of the Si/O, (C+O)/He, and He/H composition interfaces (Figure 2), the value of  $\rho r^3$  varies nonmonotonically with radius such that the shock velocity increases when the shock approaches a composition interface and decreases after the shock has crossed the interface. A deceleration of the shock causes a density inversion in the post-shock flow, which means that a dense shell forms. Such shells at the locations of the composition interfaces are subject to Rayleigh-Taylor (RT) instabilities because they are characterized by density and pressure gradients of opposite signs (Chevalier 1976).

To compare the relative strength of the growth of RT instabilities in different progenitor models, we performed an additional set of 1D neutrino-driven explosion simulations for all progenitor stars given in Table 1, using the same modeling approach as in our 3D simulations. The 1D models in this set develop approximately the same explosion energy of 1.4 B. To qualitatively analyze the RT instabilities found in our 3D simulations, we computed linear RT growth rates as a function of enclosed mass for the 1D models and integrated these rates over a period of time much longer than the time until shock breakout (roughly for a period of one day; see Figure 3). However, because RT instabilities will quickly enter the nonlinear regime in 3D simulations, the results of linear perturbation theory can only provide qualitative information on the relative strength of the expected growth of RT instabilities in different layers of the progenitor star. Nevertheless, the results turned out to be useful for a qualitative understanding of differences in the efficiency of mixing of  $^{56}\text{Ni}$  in different single-star progenitors Utrobin et al. (2019), and were useful when analyzing the results of 3D simulations.

Here we focus on the time evolution of the time-integrated RT growth factor at the He/H composition interface (Figure 4) where its value reaches a maximum in our binary-merger progenitors (Figure 3). As Utrobin et al. (2019) we consider a simple phenomenological approach to capture multidimensional effects of RT mixing at a composition interface and to describe the evolution of the nickel velocity:

$$\frac{dv}{dt} = \beta \sigma_{\text{RT}} v_0, \quad (1)$$

where  $v$  is the maximum velocity of the bulk mass of radioactive  $^{56}\text{Ni}$ ,  $\beta$  is an empirical buoyancy coefficient,  $\sigma_{\text{RT}}$  is the linear RT growth rate

$$\sigma_{\text{RT}} = \frac{1}{\rho} \sqrt{-\frac{\partial P}{\partial r} \frac{\partial \rho}{\partial r}}, \quad (2)$$

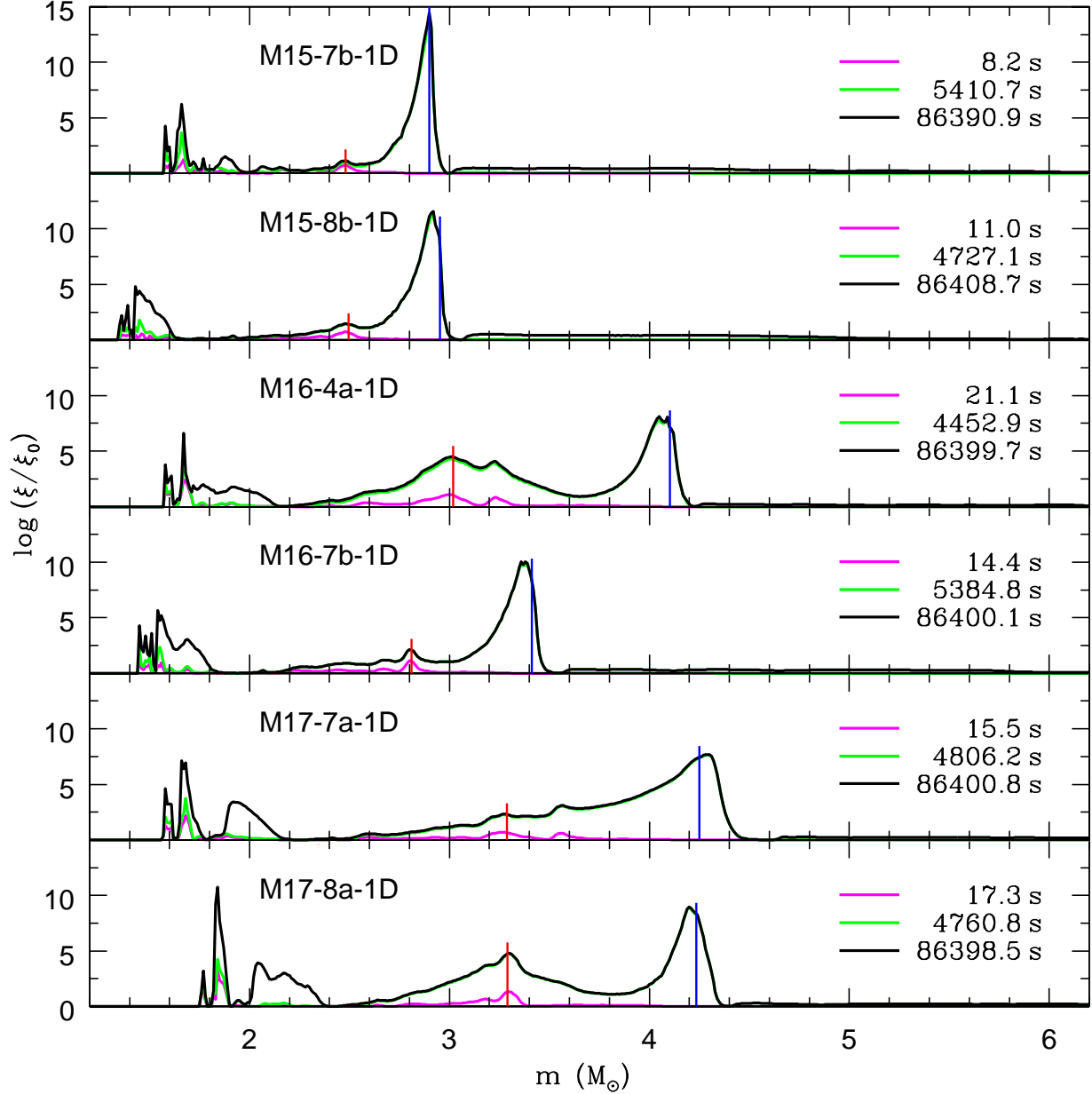


**Figure 3.** Time-integrated RT growth factors vs. enclosed mass for the 1D explosion models based on the corresponding pre-SN models M15-7b, M15-8b, M16-4a, M16-7b, M17-7a, and M17-8a at the given times. The magenta, green, and black lines show the growth factors at the time when the SN shock crosses the He/H composition interface, at the time of shock breakout, and at about one day after the onset of the explosion, respectively. The vertical red and blue lines denote the mass coordinates of the (C+O)/He and He/H composition interfaces, respectively. These interfaces are RT unstable after the passage of the SN shock.

and  $v_0$  is the initial value of the radial velocity of  $^{56}\text{Ni}$ . The solution of Equation 1 is given by

$$v(t) = \beta v_0 \int_0^t \sigma_{\text{RT}}(\tau) d\tau = \beta v_0 \ln(\xi(t)/\xi_0), \quad (3)$$

where

$$\frac{\xi}{\xi_0}(t) = \exp\left(\int_0^t \sigma_{\text{RT}}(\tau) d\tau\right) \quad (4)$$

is the time-integrated RT growth factor at time  $t$ , and  $\xi_0$  is the amplitude of the initial perturbation at a given Lagrangian

mass coordinate. Thus, the velocity growth factor  $v(t)/v_0$  at time  $t$  is proportional to the logarithm of the time-integrated RT growth factor at that time. According to Figure 4, the growth factor  $\xi(t)/\xi_0$  increases at the He/H composition interface from a value of unity shortly after the SN shock crosses this interface to its maximum (i.e., final) value at the time of shock breakout. During this time interval the growth factor approximately exhibits a power law dependence

$$\frac{\xi}{\xi_0}(t) \approx A t^\alpha, \quad (5)$$

as indicated by the linear slope of the green lines in Figure 4, and where  $A$  is a constant and  $\alpha$  is the value of the slope. This approximation implies a simple inverse time dependence of the linear RT growth rate

$$\sigma_{\text{RT}} \approx \frac{\alpha}{t}, \quad (6)$$

and hence the occurrence of a local maximum of  $\sigma_{\text{RT}}$  at a time between shortly after the SN shock crosses the He/H interface and the onset of power law growth.

Before we proceed further, let us recall the origin of the binary-merger progenitors for SN 1987A. The main element of the merger model of Menon & Heger (2017) is merging of a main-sequence secondary star with a RSG primary star in the common-envelope phase when the secondary eventually penetrates the helium core of the primary. The helium core of the resulting merged star inherits the basic property of the RSG primary star evolved as a single star: its density profile is characterized by a low time-integrated RT growth factor near the (C+O)/He composition interface and a very large one at the He/H interface, since the density gradient at the He/H interface is much steeper than at the (C+O)/He interface (Figures 1 and 3). In contrast, the single-star BSG progenitors for SN 1987A demonstrate opposite behavior: a large time-integrated RT growth factor near the (C+O)/He composition interface and a low one at the He/H interface (Utrobín et al. 2019).<sup>4</sup>

This fundamental difference between BSG and RSG progenitors concerning the RT growth factors at the (C+O)/He and He/H interfaces was previously pointed out by Wongwathanarat et al. (2015), and the general properties of radial mixing in the ejecta induced by the 3D neutrino-driven explosions were studied. It was shown that the extent of radial mixing, i.e., the minimum velocity of hydrogen-rich matter and the maximum velocity of  $^{56}\text{Ni}$ , depends not only on the initial asphericity and explosion energy, but also on the density profiles and widths of the C+O core and the helium shell, and on the density gradient at the He/H composition interface. A dominant growth rate at the He/H interface in the RSG explosions compared to the BSG cases gives rise to a more strongly RT-unstable layer after the passage of the SN shock, which then develops into more extended inward mixing of hydrogen into the helium core than in the BSG explosions. On the other hand, a dominant growth rate at the (C+O)/He interface in the BSG explosions compared to the RSG ones results in a relatively strong outward mixing of  $^{56}\text{Ni}$  in velocity space, which turns out to be comparable to that in the RSG ejecta, where the extended fast  $^{56}\text{Ni}$ -rich fingers have more time to grow, because the reverse shock at

the He/H interface develops at a much larger radius and thus much later than in the BSG progenitors.

The above findings concerning the inward mixing of hydrogen and the outward mixing of radioactive  $^{56}\text{Ni}$  are confirmed by the 3D neutrino-driven explosion simulations based on the single-star progenitors for SN 1987A (BSG pre-SN models except for model N20 in Utrobín et al. 2019) and the binary-merger progenitors (pre-SN models with the RSG-like helium cores, see Figures 1 and 3). Explosions of the single-star BSG progenitors with SN 1987A-like energies show that hydrogen-rich matter mixed into the helium core expands with velocities from  $270 \text{ km s}^{-1}$  to  $1850 \text{ km s}^{-1}$ , and its mass does not exceed  $0.15 M_{\odot}$  (Utrobín et al. 2019). In turn, all hydrodynamic models based on the binary-merger progenitors demonstrate that hydrogen is mixed more deeply into the helium core down to velocities lower than  $40 \text{ km s}^{-1}$ , and its mass constitutes about  $0.5 M_{\odot}$  (Table 2). As to the outward mixing of  $^{56}\text{Ni}$ , our favorite hydrodynamic models B15-2, based on the single-star progenitor (Utrobín et al. 2019), and M15-7b-3, based on the binary-merger progenitor (Table 2), have nearly the same maximum velocities of the bulk of  $^{56}\text{Ni}$  consistent with the observed value of about  $3000 \text{ km s}^{-1}$ .

### 3.3. 3D morphology of explosion models

Let us first consider the reference 3D explosion models M15-7b-3, M15-8b-1, M16-4a-1, M16-7b-2, M17-7a-2, and M17-8a-4, which explode with comparable energies (Table 2). The SN shock wave first crosses the Si/O interface and then reaches the (C+O)/He interface, at which time the maximum speed of the bulk mass of the  $^{56}\text{Ni}$ -rich matter,  $v_{\text{Ni}}^{\text{CO}}$ , spreads over a rather wide range from  $9210 \text{ km s}^{-1}$  to  $14380 \text{ km s}^{-1}$  (Table 3; first and third columns in Figure 5), depending on the progenitor. At this stage the nickel-rich ejecta consist of plume-like or bubble-like structures, some of which move outward with relatively high velocities compared to others. Note that during this phase the maximum radial velocities of these structures are larger than the average velocity of the SN shock in models M15-7b-3, M16-4a-1, and M17-8a-4, and, in contrast, are lower in models M15-8b-1, M16-7b-2, and M17-7a-2 (Figure 4). Figure 4 also shows that in the first three models the average shock velocity and the maximum radial velocity on the surface where the mass fraction of  $^{56}\text{Ni}$  plus neutron-rich tracer nucleus equals 3% are most similar (even equal in models M15-7b-3 and M17-8a-4) at the time when the shock crosses the He/H interface. After the SN shock has passed the He/H interface, a reverse shock forms below the He/H interface. In models M15-7b-3, M16-4a-1, and M17-8a-4 a few fastest RT plumes expanding with increasing speed begin to decelerate shortly after the forward shock has entered the helium shell. They remain close to the forward shock, and, consequently, avoid strong decel-

<sup>4</sup> The only exception to this is model N20, which originates from a RSG progenitor rather than a BSG star with respect to the structure of the helium core (Nomoto & Hashimoto 1988; Saio et al. 1988).

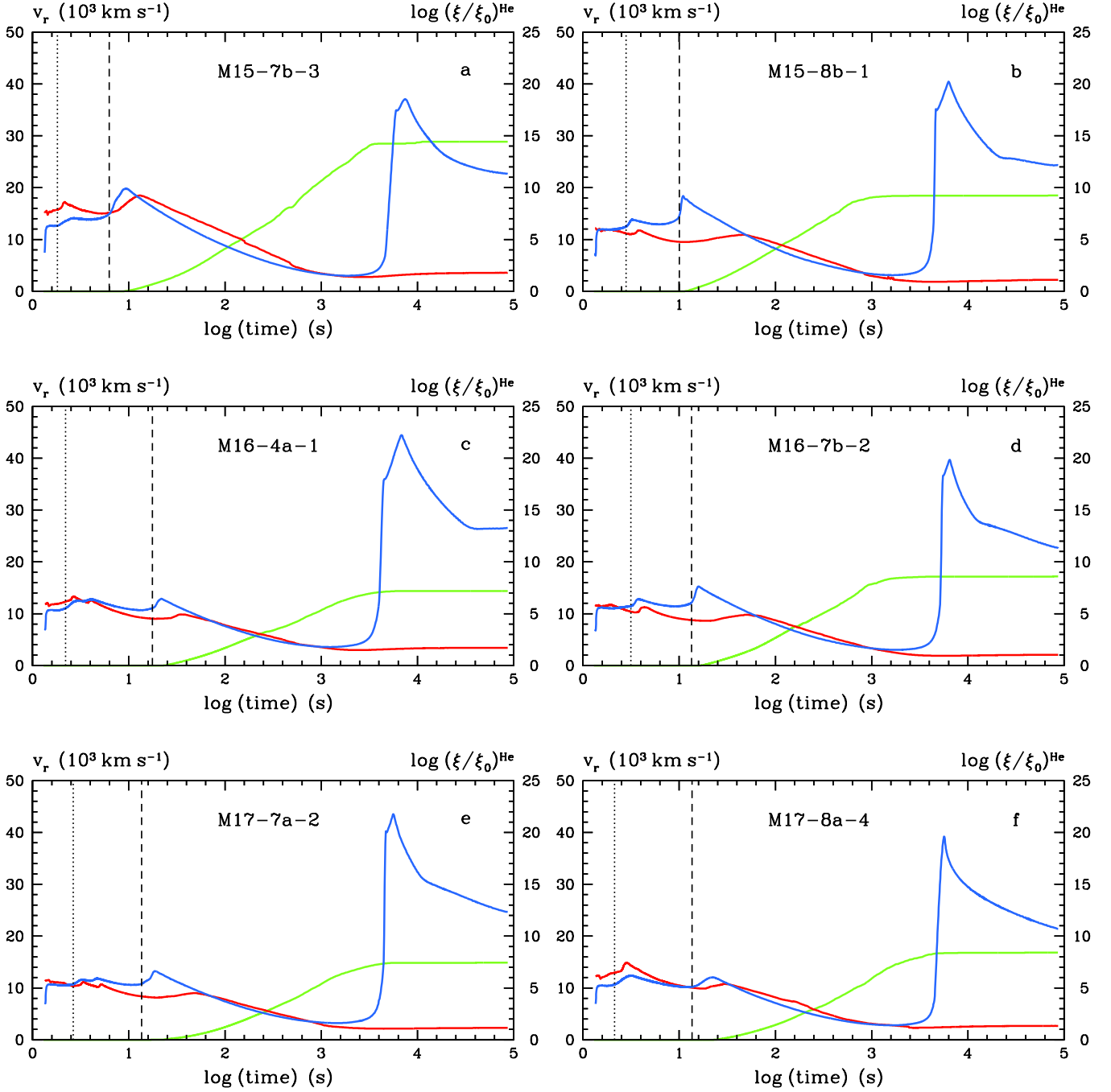


**Figure 4.** Time evolution of the angle-averaged radial velocity of the SN shock (blue lines) and the maximum radial velocity on the surface where the mass fraction of  $^{56}\text{Ni}$  plus the neutron-rich tracer nucleus equals 3% (red lines) for our six reference 3D explosion models M15-7b-3, M15-8b-1, M16-4a-1, M16-7b-2, M17-7a-2, and M17-8a-4, and the time-integrated RT growth factor at the He/H composition interface (green lines) for the same models simulated in 1D. The vertical dotted and dashed lines mark the times when the shock crosses the (C+O)/He and He/H composition interfaces, respectively. The former times are identical to those of the snapshots shown in columns one and three of Figure 5.



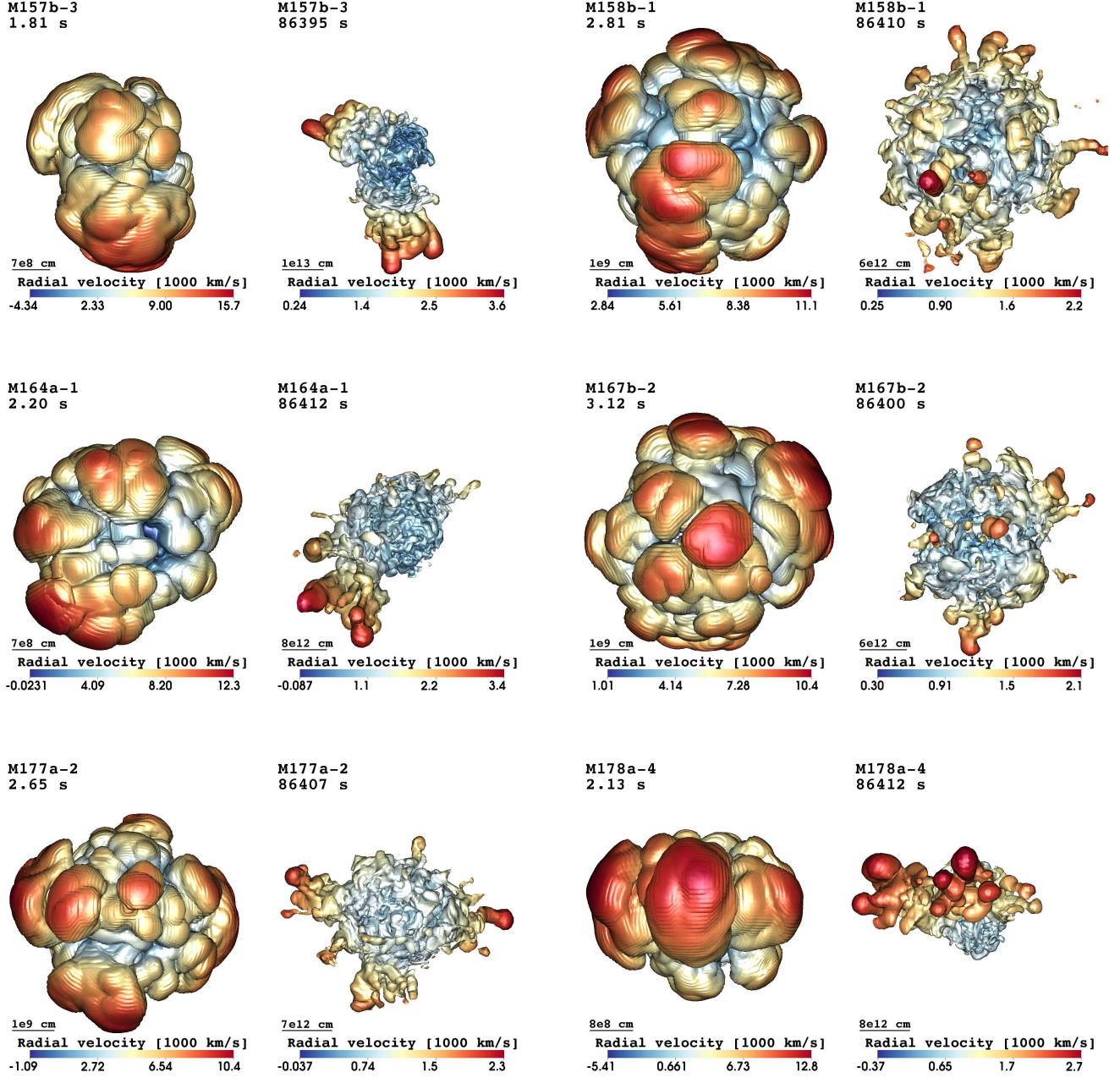


**Figure 5.** Morphology of radioactive  $^{56}\text{Ni}$ -rich matter produced by iron-group nucleosynthesis in shock-heated and neutrino-heated ejecta. The snapshots display isosurfaces where the mass fraction of  $^{56}\text{Ni}$  plus the neutron-rich tracer nucleus equals 3%. The isosurfaces are shown for our six reference 3D explosion models at two different epochs: shortly before the SN shock crosses the (C+O)/He composition interface in the progenitor star (first and third columns), and long after shock breakout (second and fourth columns). In the top left corner of each panel, we give the name of the model and the post-bounce time of the snapshot. The colors represent the radial velocity on the isosurface, and the color-coding is defined at the bottom of each panel. The size of the displayed volume and of the plume-like structures can be estimated from the yardsticks given in the lower left corner of each panel. There are striking differences in the final morphology of the  $^{56}\text{Ni}$ -rich ejecta between these models, all of which have comparable and effectively SN 1987A-like explosion energies. These differences arise from progenitor-specific differences in their stellar density and composition structures, and from the influence of the latter on the unsteady SN shock propagation. From an inspection of the final morphology, it is possible to distinguish two groups of models: M15-8b-1, M16-7b-2, and M17-7a-2 with a small asphericity and M15-7b-3, M16-4a-1, and M17-8a-4 with a large asphericity.

eration by the reverse shock, because they propagate ahead of the location where the reverse shock forms (Figure 6). As a result, the fastest  $^{56}\text{Ni}$ -rich clumps move with velocities of about  $2780 \text{ km s}^{-1}$ ,  $3140 \text{ km s}^{-1}$ , and  $3630 \text{ km s}^{-1}$  at late times in models M17-8a-4, M16-4a-1, and M15-7b-3, respectively (Figure 5, second and fourth columns; Figure 7). In contrast, in models M16-7b-2, M15-8b-1, and M17-7a-2 the  $^{56}\text{Ni}$ -rich plumes collide with the reverse shock, move well behind the forward shock (Figure 6), and are compressed in the dense shell that piles up between the forward and reverse shocks. Thus they exhibit a considerably more isotropic overall shape with a much lower velocity contrast between the fastest and slowest structures (Figure 5, second and fourth columns). In models M16-7b-2, M15-8b-1, and M17-7a-2 the peak velocities are only about  $2030 \text{ km s}^{-1}$ ,  $2200 \text{ km s}^{-1}$ , and  $2280 \text{ km s}^{-1}$ , respectively (Figure 7).

A striking difference in the final morphology of the  $^{56}\text{Ni}$ -rich ejecta results in our reference 3D explosion models (Figure 5, second and fourth columns) from the different structures of the binary-merger progenitors (Figure 1), and their influence on the unsteady SN shock propagation and the development of RT instabilities at the (C+O)/He and He/H composition interfaces (Figure 3). The final morphology of models M15-8b-1, M16-7b-2, and M17-7a-2 (the first group) exhibits a small asphericity in contrast to models M15-7b-3, M16-4a-1, and M17-8a-4 (the second group) which are largely aspherical. This difference may be interpreted as a consequence of the different strength of the interaction between the  $^{56}\text{Ni}$ -rich ejecta and the reverse shock at the He/H composition interface. In reality, the extent of  $^{56}\text{Ni}$  mixing, measured by the dimensionless ratio of the maximum velocity of the bulk mass of  $^{56}\text{Ni}$  ejecta to the mean velocity of the bulk mass of  $^{56}\text{Ni}$  (averaged with the  $^{56}\text{Ni}$  mass fraction as weight function) increases from the first to the second group of models (Figure 7, Table 3). In other words, the degree of asymmetry in the final morphology of the  $^{56}\text{Ni}$ -rich ejecta correlates with the extent of  $^{56}\text{Ni}$  mixing in velocity space.

### 3.4. Variations of explosion energy and stochasticity

3D neutrino-driven explosion simulations of SN 1987A based on the single-star pre-SNe showed that the extent of  $^{56}\text{Ni}$  mixing, measured by the maximum radial velocity of the bulk mass of the  $^{56}\text{Ni}$ -rich ejecta, is proportional to the explosion energy (Utrobin et al. 2015, 2019). Such a correlation is also observed for 3D neutrino-driven explosion simulations based on the binary-merger pre-SNe with some exceptions (Table 2). The most prominent exception is demonstrated by models M15-7b-1, M15-7b-2, M15-7b-3, and M15-7b-4 which are based on the same progenitor model M15-7b and explode with a monotonically growing energy (Table 2). This sequence of models provides an opportunity to explore the dependence of their mixing properties not only on the explo-

sion energy itself, but also in models exploding with sufficiently similar energies, on the initial asymmetry of the  $^{56}\text{Ni}$ -rich ejecta, created by the stochastic growth of convective and SASI mass motions. In order to realize this opportunity, we analyze the time evolution of the radial velocity of the SN shock and the maximum radial velocity of the radioactive  $^{56}\text{Ni}$ -rich ejecta (Figure 8) and the morphology of this matter (Figure 9).

Models M15-7b-1 and M15-7b-4 have considerably different explosion energies and obey the mentioned correlation between the explosion energy and the extent of  $^{56}\text{Ni}$  mixing (Table 2). Accordingly, the average velocity of the SN shock and the maximum radial velocity of the  $^{56}\text{Ni}$ -rich ejecta are both higher at all times in the more energetic explosion of model M15-7b-4 compared to model M15-7b-1 (Figure 8). We then focus on the interesting results obtained for models M15-7b-2 and M15-7b-3 exploding with nearly the same energies of 1.428 B and 1.432 B, but whose  $^{56}\text{Ni}$ -rich ejecta are mixed to quite different maximum velocities of the bulk mass of  $^{56}\text{Ni}$  of  $3406 \text{ km s}^{-1}$  and  $2980 \text{ km s}^{-1}$ , respectively (Table 2). Such a significant difference in the maximum velocity of the bulk mass of  $^{56}\text{Ni}$  cannot be explained by a negligible difference in the explosion energy.

Along with the explosion energy, the initial asymmetry of the  $^{56}\text{Ni}$ -rich ejecta is another important property of SN explosions that determines the maximum radial velocity of  $^{56}\text{Ni}$ -rich ejecta. Wongwathanarat et al. (2015) found that there is a clear correlation between the asymmetries of the  $^{56}\text{Ni}$ -rich ejecta at late times and the early-time asymmetries originating from hydrodynamic instabilities generated during the onset of the SN explosion. In other words, the fundamental features of the morphology of the  $^{56}\text{Ni}$ -rich ejecta are imprinted by the “neutrino engine” during the first second of the explosion. When the SN shock approaches the (C+O)/He composition interface, the maximum radial velocity of the  $^{56}\text{Ni}$ -rich ejecta in model M15-7b-2 exceeds that of model M15-7b-3 (Figure 8) despite their practically equal explosion energies (Table 2). This fact may be interpreted in terms of a specific morphology of the  $^{56}\text{Ni}$ -rich ejecta in these models, which is seeded by different random perturbations and amplified by the stochastic growth of the hydrodynamic instabilities in the neutrino-heating layer. Inspecting the early-time morphology of the  $^{56}\text{Ni}$ -rich ejecta of models M15-7b-2 and M15-7b-3 in Figure 9, we see large mushroom-head-like structures in directions of the biggest initial convective plumes observed at the onset of the explosion. These mushroom heads are more prominent and faster in model M15-7b-2 than in M15-7b-3. At late times these large-scale, coherent structures have grown to extended RT fingers with the maximum speed of the bulk mass of the  $^{56}\text{Ni}$ -rich matter in model M15-7b-2 being larger than that in model M15-7b-3, similar to the situation at early times. This essential prop-

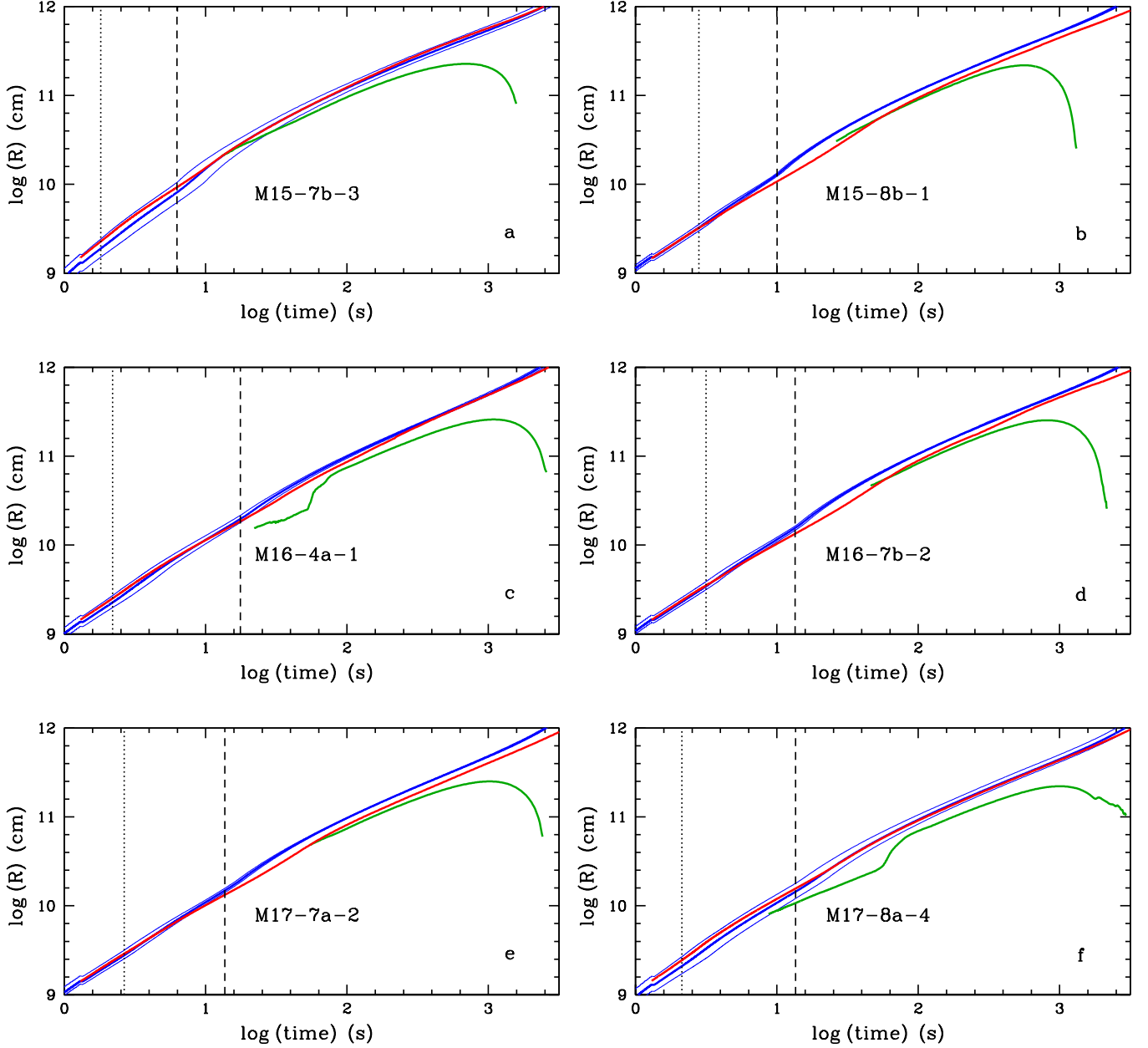


**Figure 6.** Time evolution of the angle-averaged radius of the SN shock (blue thick lines), the minimum and maximum radii of the SN shock (blue thin lines), the angle-averaged radius of the reverse shock (green lines), and the maximum radius on the surface where the mass fraction of  $^{56}\text{Ni}$  plus neutron-rich tracer nucleus equals 3% (red lines) for our six reference 3D explosion models M15-7b-3, M15-8b-1, M16-4a-1, M16-7b-2, M17-7a-2, and M17-8a-4. See caption of Figure 4 for details.

erty and difference between models M15-7b-2 and M15-7b-3 is facilitated by the fact that the fast RT plumes in model M15-7b-2 enter the helium shell earlier than in M15-7b-3, which is indicated by the earlier deceleration of the  $^{56}\text{Ni}$ -rich ejecta in model M15-7b-2. Consequently, the RT plumes are closer to the SN shock in model M15-7b-2 and undergo a weaker interaction with the reverse shock that forms below the He/H composition interface (Figure 8). Thus, a comparison of models M15-7b-1, M15-7b-2, M15-7b-3, and M15-7b-4 leads to the generalized conclusion that the maximum

velocity of the bulk mass of  $^{56}\text{Ni}$  is proportional to the explosion energy with some stochastic uncertainty for a given progenitor model.

The morphology of the  $^{56}\text{Ni}$ -rich ejecta in models M15-7b-1, M15-7b-2, M15-7b-3, and M15-7b-4 (Figure 9) exploding with a monotonically growing energy (Table 2) confirms two previous findings. First, these models demonstrate the correlation between the early-time asymmetries of the  $^{56}\text{Ni}$ -rich ejecta and the asymmetries at late times discussed already by [Wongwathanarat et al. \(2015\)](#). Second, the size of the asym-

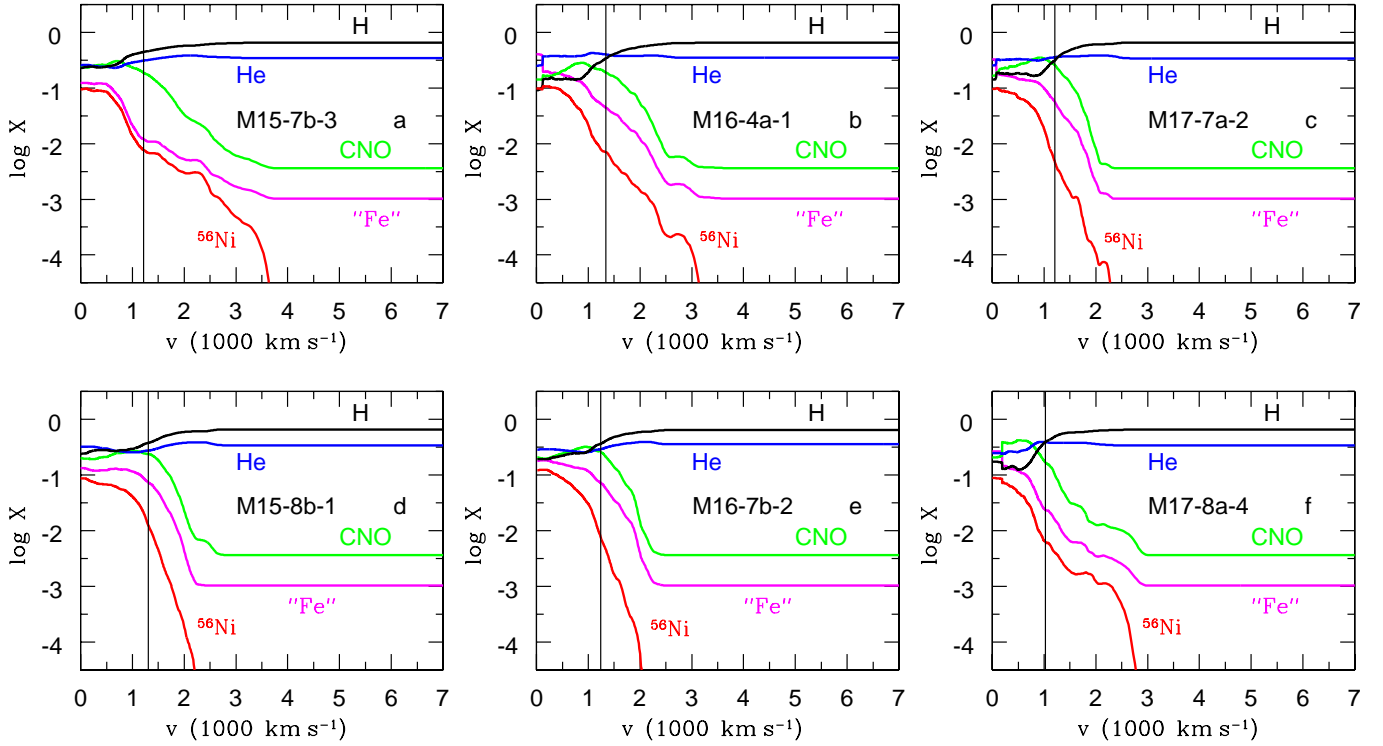


**Figure 7.** Mass fractions of hydrogen (black line), helium (blue line), CNO group elements (green line), iron group elements except for <sup>56</sup>Ni (magenta line), and radioactive <sup>56</sup>Ni (red line) as functions of velocity at day 50 in models M15-7b-3 (a), M16-4a-1 (b), M17-7a-2 (c), M15-8b-1 (d), M16-7b-2 (e), and M17-8a-4 (f) (Table 2). Thin vertical lines indicate ejecta velocities at the location of the outer edge of the pre-SN helium cores.

metry at early times correlates with the degree of asymmetry in the final morphology of the <sup>56</sup>Ni-rich ejecta, which in turn correlates with the extent of <sup>56</sup>Ni mixing in velocity space: the global deformation of M15-7b-1 is much less extreme, models M15-7b-2 and M15-7b-3 have a very pronounced asphericity with a bipolar elongation, and the morphology of model M15-7b-4 is distinguished by a strongly one-sided distribution of the <sup>56</sup>Ni-rich ejecta, suggesting a large dipole asymmetry of the SN shock at the onset of the explosion.

### 3.5. Extent of <sup>56</sup>Ni mixing and properties of progenitors

Utrobin et al. (2019) interpreted the complex phenomenon of RT mixing (see Section 3.2) in a simple phenomenological approach and found that the efficiency of outward radioactive <sup>56</sup>Ni mixing in the framework of the 3D neutrino-driven simulations depends mainly on the following two hydrodynamic properties of the single-star BSG progenitor models: a high growth factor of RT instabilities at the (C+O)/He composition interface, and a weak interaction of fast RT plumes with the reverse shock occurring below the He/H composition interface. It is interesting now to carry out a similar analysis of the binary-merger progenitors which have a RSG-like structure inside the He/H composition interface of their primaries.

This phenomenological approach attempts to capture multidimensional effects of RT mixing at the (C+O)/He compo-

sition interface by describing the evolution of the <sup>56</sup>Ni velocity by means of a velocity growth factor which is proportional to the logarithm of the time-integrated RT growth factor (see Equation 3). To this end, we calculated the maximum (i.e., final) value of this growth factor,  $(\xi/\xi_0)^{\text{CO}}$ , in the close vicinity of the (C+O)/He composition interface (Figure 3, Table 3).

The fast RT plumes that grow from the C+O core outward through the helium shell can interact with the reverse shock developing below the He/H composition interface. Whether such an interaction happens depends on the ratio of two timescales, namely (1) the time it takes to form the reverse shock, after the SN shock has crossed the He/H composition interface,  $t_{\text{RS}}$ , and (2) the time needed by RT plumes originating from the (C+O)/He interface to reach the radius,  $R_{\text{RS}}$ , where the reverse shock forms. The latter timescale is given by the ratio of  $R_{\text{RS}}$  and the maximum velocity of the bulk mass of <sup>56</sup>Ni when the SN shock passes the (C+O)/He composition interface,  $v_{\text{Ni}}^{\text{CO}}$ , multiplied by the growth factor  $(\xi/\xi_0)^{\text{CO}}$ , which takes into account the subsequent evolution of this velocity.

The greater the ratio of the two timescales, the weaker the interaction and the higher the terminal velocity of fast RT plumes in the hydrogen envelope. In Table 3 we give the corresponding quantities that determine the amount of mixing of radioactive <sup>56</sup>Ni for all binary-merger models.



**Table 3.**  $^{56}\text{Ni}$  mixing and hydrodynamic properties of binary-merger progenitors

Model	$M_{\text{He}}^{\text{core}}$	$t^{\text{CO}}$	$t^{\text{He}}$	$\langle v \rangle_{\text{Ni}}^{150}$	$v_{\text{Ni}}^{150}$	$v_{\text{Ni}}^{\text{CO}}$	$\log(\xi/\xi_0)^{\text{CO}}$	$\log(\xi/\xi_0)^{\text{He}}$	$t_{\text{RS}}$	$R_{\text{RS}}$
	( $M_{\odot}$ )	(s)		( $10^3 \text{ km s}^{-1}$ )					(s)	( $R_{\odot}$ )
M15-7b-1	2.90	1.933	6.46	1.344	2.629	14.51	1.16	14.4	19.0	0.607
M15-7b-2	2.90	1.844	6.58	1.351	2.954	14.38	1.16	14.4	18.9	0.605
M15-7b-3	2.90	1.814	6.26	1.364	2.579	14.83	1.16	14.4	18.9	0.606
M15-7b-4	2.90	1.668	5.64	1.500	3.344	16.36	1.16	14.4	17.5	0.600
M15-8b-1	2.95	2.811	10.03	0.992	1.609	9.78	1.48	11.6	10.6	0.559
M15-8b-2	2.95	3.041	11.39	0.816	1.282	8.32	1.48	11.6	11.5	0.556
M16-4a-1	4.10	2.200	17.63	0.951	1.997	10.79	4.49	8.1	35.9	1.049
M16-4a-2	4.10	2.276	19.14	0.790	1.721	10.07	4.49	8.1	41.3	1.059
M16-7b-1	3.41	3.301	14.24	0.811	1.356	8.74	2.15	10.0	20.4	0.791
M16-7b-2	3.41	3.154	13.45	0.881	1.485	9.42	2.15	10.0	18.2	0.760
M17-7a-1	4.25	2.659	13.82	0.831	1.526	9.21	2.32	7.7	28.6	0.890
M17-7a-2	4.25	2.653	13.64	0.819	1.446	9.21	2.32	7.7	28.3	0.889
M17-8a-3	4.23	2.064	13.87	0.941	2.068	11.12	4.80	9.0	45.1	1.003
M17-8a-4	4.23	2.130	13.58	0.943	2.147	11.09	4.80	9.0	43.2	1.001

NOTE—Columns 1 and 2 give the name of the 3D hydrodynamic explosion model and the helium-core mass of the corresponding pre-SN model. Columns 3 and 4 list the times when the SN shock in the 3D explosion models crosses the C+O/He and He/H composition interfaces, respectively. Columns 5, 6, and 7 provide the averaged characteristic velocities for the bulk of  $^{56}\text{Ni}$  containing 96% of the total  $^{56}\text{Ni}$  mass in the 3D simulations:  $\langle v \rangle_{\text{Ni}}^{150}$  is the mean velocity of the bulk mass of  $^{56}\text{Ni}$ , averaged with the  $^{56}\text{Ni}$  mass fraction as weight function at day 150;  $v_{\text{Ni}}^{150}$  is the maximum velocity of the bulk mass of  $^{56}\text{Ni}$  at the same epoch; and  $v_{\text{Ni}}^{\text{CO}}$  is the maximum velocity of the bulk mass of  $^{56}\text{Ni}$  at the moment just after the SN shock has passed the (C+O)/He composition interface. Columns 8 – 11 give hydrodynamic properties of 1D explosion models:  $(\xi/\xi_0)^{\text{CO}}$  and  $(\xi/\xi_0)^{\text{He}}$  are the maximum time-integrated RT growth factors in the close vicinity of the (C+O)/He and He/H composition interfaces, respectively (Figure 3);  $t_{\text{RS}}$  is the formation time of the reverse shock below the He/H composition interface, which is measured from the moment when the SN shock crosses this composition interface; and  $R_{\text{RS}}$  is the radius of the reverse shock at the formation epoch.

Following Utrobin et al. (2019), we measure the extent of  $^{56}\text{Ni}$  mixing by the dimensionless ratio of the maximum velocity of the bulk mass of  $^{56}\text{Ni}$  ejecta containing 96% of the total  $^{56}\text{Ni}$  mass at day 150,  $v_{\text{Ni}}^{150}$ , to the weighted mean velocity of the bulk mass of  $^{56}\text{Ni}$  at the same epoch,  $\langle v \rangle_{\text{Ni}}^{150}$ , whereby we eliminate the influence of slightly different explosion energies of the models. Because the outward mixing of  $^{56}\text{Ni}$  depends on the growth factor of RT plumes at the (C+O)/He composition interface as well as on the interaction of those plumes with the reverse shock from the He/H composition interface, we use the product of the corresponding growth factors (as explained above) on the abscissa in Figure 10(c). For comparison, we provide the corresponding plot for the single-star models in Figure 10(d). From an inspection of these figures, it is evident that both the reference binary-merger models and the single-star models exhibit in a quite similar way a correlation between the extent of outward radioactive  $^{56}\text{Ni}$  mixing and the hydrodynamic explosion properties linked to the structure of the progenitor mod-

els. But there are two relevant exceptions. First, the binary-merger model M15-7b-3 lies well above the correlation relation suggested by Figure 10(c). Second, the single-star model N20 lies far off the correlation suggested by Figure 10(d).

At this point let us recall that the progenitor model M15-7b has the largest time-integrated RT growth factor near the He/H composition interface among all binary-merger progenitor models under consideration (Figure 3 and Table 3), and the single-star progenitor model N20 is a RSG progenitor rather than a BSG one with respect to the structure of the helium core as we have pointed out before. Hence, the locations of these models off the expected correlation lines in Figures 10(c) and (d) might suggest a noticeable influence of the high growth factor of RT instabilities at the He/H composition interface on the outward mixing of radioactive  $^{56}\text{Ni}$ . In other words, we have to perform a more careful analysis to account for this influence and to further improve the correlations between nickel mixing and explosion properties of binary-merger and single-star progenitors, respectively.

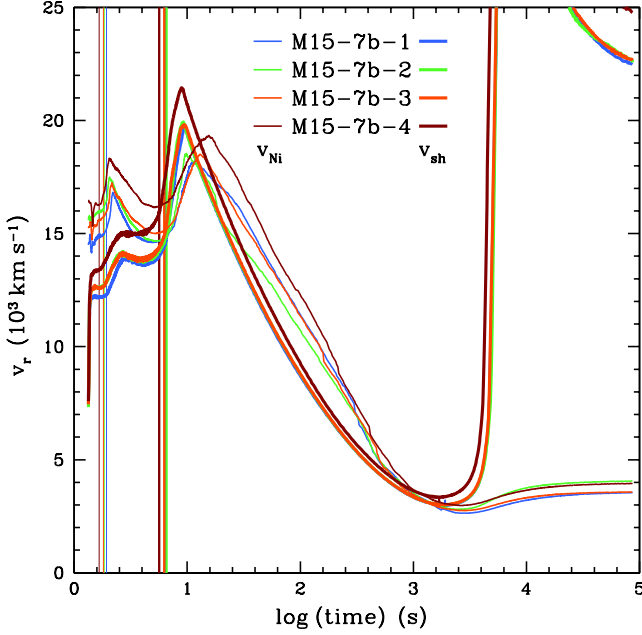


**Figure 8.** Time evolution of the average velocity of the SN shock,  $v_{\text{sh}}$  (thick lines), and of the maximum radial velocity on the surface where the mass fraction of  $^{56}\text{Ni}$  plus the neutron-rich tracer nucleus equals 3%,  $v_{\text{Ni}}$  (thin lines), for models M15-7b-1, M15-7b-2, M15-7b-3, and M15-7b-4. The vertical thin and thick lines mark the times when the shock crosses the (C+O)/He and He/H composition interfaces, respectively.

In our phenomenological approach, which captures multidimensional effects of RT mixing at a composition interface and describes the evolution of the nickel velocity (Equation 3), the terminal maximum velocity of the bulk mass of radioactive  $^{56}\text{Ni}$  is proportional to the natural logarithm of the time-integrated RT growth factor at this interface and to the initial value of the radial velocity of  $^{56}\text{Ni}$ . Considering the mixing processes around the He/H composition interface, it is therefore natural to use the velocity of the bulk mass of  $^{56}\text{Ni}$  – which results from the acceleration of nickel-rich RT plumes at the (C+O)/He interface and their subsequent interaction with the reverse shock from the He/H interface (both are accounted for by the quantity on the horizontal axis of Figures 10(c) and (d)) – as the initial value of the radial velocity of  $^{56}\text{Ni}$  at the He/H interface in Equation 3. Thus, multiplying the quantity at the abscissa of Figures 10(c) and (d) by the logarithm of the time-integrated RT growth factor at the He/H composition interface, we reasonably estimate the effect of a high growth factor at this interface on the extent of outward mixing of radioactive  $^{56}\text{Ni}$ .

The results of this procedure are shown in Figures 10(a) and (b) for the binary-merger and single-star explosion models, respectively. We find a much better correlation between the normalized extent of  $^{56}\text{Ni}$  mixing and the product of the three hydrodynamic properties that favor the mixing of ra-

dioactive  $^{56}\text{Ni}$  during the explosions of the different progenitors. Our modified measure for the efficiency of  $^{56}\text{Ni}$  mixing moves the locations of both the binary-merger model M15-7b-3 and the single-star model N20 to the ideal, linear correlation lines plotted in green. The existence of these correlations confirms the decisive role of the three considered factors for the outward mixing of radioactive  $^{56}\text{Ni}$  during 3D neutrino-driven SN simulations of binary-merger and single-star progenitors.

Note that the growth factors at the (C+O)/He and He/H composition interfaces alone cannot explain the final  $^{56}\text{Ni}$ -mixing velocities because they result in a weak correlation with significant scatter for both the binary-merger and single-star models as it is shown in Figures 10(e) and (f), respectively. At the same time, this kind of plot can give a crude and a priori (i.e., without any information from 3D simulations) estimate of the maximum velocity of the bulk mass of radioactive  $^{56}\text{Ni}$  in explosions of different progenitors on the basis of – and this is the important point here – only the growth factors (derived from linear theory) of RT instabilities at the composition interfaces after shock passage.

From an inspection of Figures 10(a) and (b), it is evident that both the binary-merger and single-star progenitors obey a correlation between the extent of outward radioactive  $^{56}\text{Ni}$  mixing and the product of the hydrodynamical quantities on the abscissa equally well. The dimensionless extent of  $^{56}\text{Ni}$  mixing varies within 1.6–2.3 and 1.4–2.4, respectively, and the values on the abscissa fall into two non-overlapping intervals of 4.5–30 and 36–127. The slopes of the correlation lines are 0.026 and 0.010 for the reference binary-merger and single-star models, respectively. The significant difference between both the abscissa values and the slopes of the correlation functions is presumably related to the fact that we only performed a scaling analysis of the outward mixing of radioactive  $^{56}\text{Ni}$  during 3D neutrino-driven simulations. The difference might be eliminated by a more detailed theory that is able to predict the dependence of the mixing efficiency on the relevant hydrodynamical properties in a quantitative manner.

Utrobín et al. (2019) showed that their set of BSG explosion models based on single-star progenitors exhibits  $^{56}\text{Ni}$  mixing with an efficiency that scales roughly inversely with the helium-core mass, which varied from  $4.05 M_{\odot}$  to  $7.40 M_{\odot}$ , i.e., having a spread of  $3.35 M_{\odot}$  (see the numbers next to the model names in Figure 10(b)). In contrast, the binary-merger models in Figure 10(a) fail to reveal any clear correlation between the amount of radial mixing of radioactive  $^{56}\text{Ni}$  and the helium-core mass of the progenitor model, which for the considered binary progenitors varies only within  $2.90 - 4.25 M_{\odot}$ , i.e., having a spread of only  $1.35 M_{\odot}$ . The latter spread might be too narrow for detecting such a correlation. However, it is possible to assert that

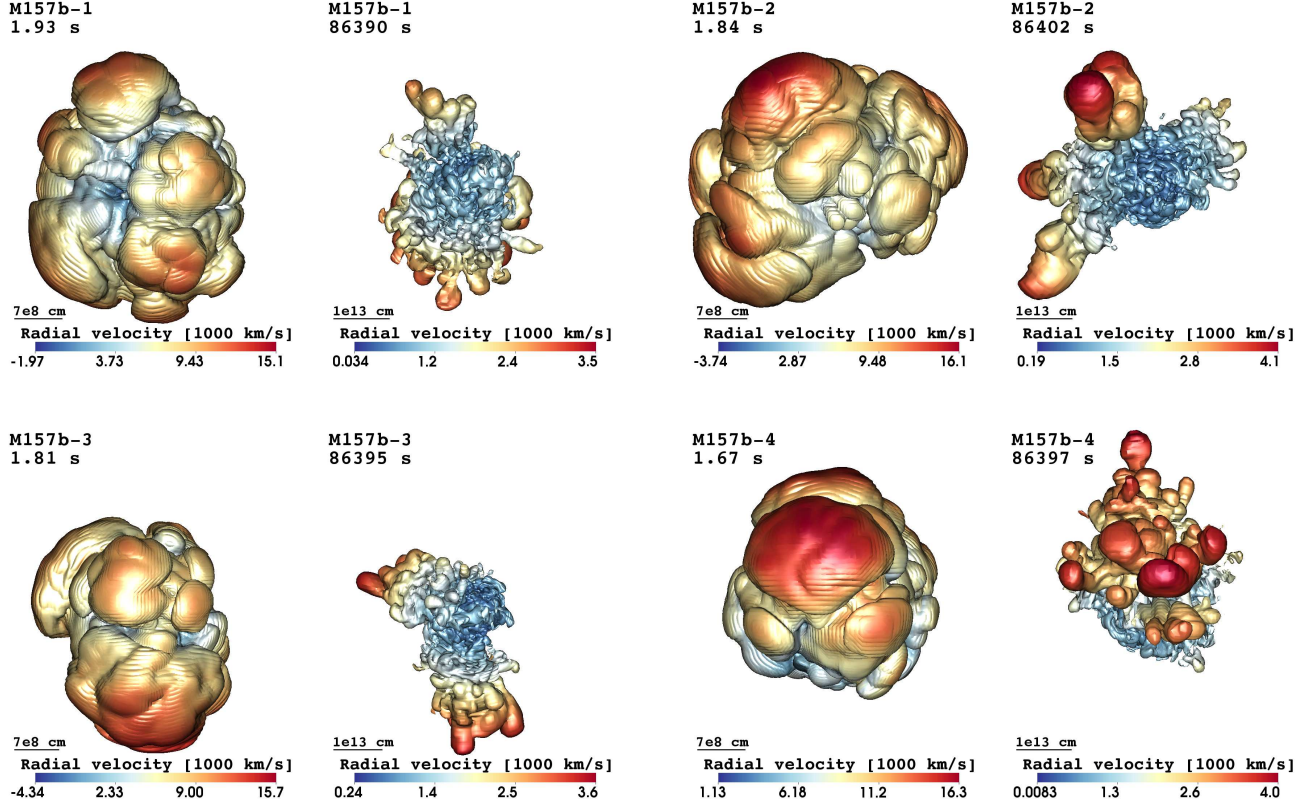


**Figure 9.** Morphology of radioactive  $^{56}\text{Ni}$ -rich ejecta in models M15-7b-1, M15-7b-2, M15-7b-3, and M15-7b-4. See caption of Figure 5 for details.

a decrease in the fraction of the He core of the primary that was dredged up,  $f_c$ , from 17.5% to 3.3% (in models M15-8b-1, M16-7b-2, M17-8a-4, and M16-4a-1) results in a growth of both the He-shell mass,  $M_{\text{He}}^{\text{shell}}$ , and the width of this shell,  $\Delta R_{\text{He}}^{\text{shell}}$ , (Table 1), and it also correlates with the extent of  $^{56}\text{Ni}$  mixing in velocity space (Figure 10(a)).

### 3.6. Light-curve modeling

The results of our light-curve modeling based on the averaged 3D explosion simulations are illustrated by the bolometric light curves (Figure 11). They depend on the relevant basic properties of the progenitors (Table 1) and 3D explosion models (Table 2), and on the distributions of chemical composition in velocity space (Figure 7). In the context of the light-curve modeling, the structure of the outermost layers is responsible for the amplitude and width of the initial luminosity peak which forms during shock breakout from the stellar surface and the subsequent adiabatic cooling phase. Analyzing both photometric and spectroscopic observations of SN 1987A, especially the sensitivity of the width of the initial peak to the radius of the pre-SN, Utrobin (2005) found that the radius is  $35 \pm 5 R_{\odot}$ . The pre-SN radii of all binary-merger models considered in our study (Table 1) fall in this

range and guarantee a good description of the initial luminosity peak during the first  $\sim 7$  days (Figure 11).

Utrobin et al. (2015) studied the influence of the explosion energy and the ejected  $^{56}\text{Ni}$  mass on the calculated light curves for the 3D explosion models based on the single-star progenitors. All models in Figure 11 show the influence of the explosion energy on the calculated light curve for the explosions of the different binary-merger progenitors, except for two model pairs (M15-7b-2, M15-7b-3) and (M17-7a-1, M17-7a-2) with almost equal explosion energies. It is well known that from about day 7 to day 30 the bolometric light curve is mainly determined by the properties of a cooling and recombination wave (CRW): the higher the ratio of explosion energy and ejecta mass, the higher the luminosity in the CRW phase because the ejecta expand and cool more quickly (cf. Utrobin et al. 2015).

After the CRW stage, when radiative diffusion takes place, the radioactive decay of  $^{56}\text{Ni}$  and  $^{56}\text{Co}$  nuclides becomes dominant in powering the luminosity. Now the bolometric light curve depends on the amount of radioactive material and its distribution over the ejecta for a given progenitor. In other words, there is an indirect influence of the explosive nucleosynthesis and mixing processes during the explosion on

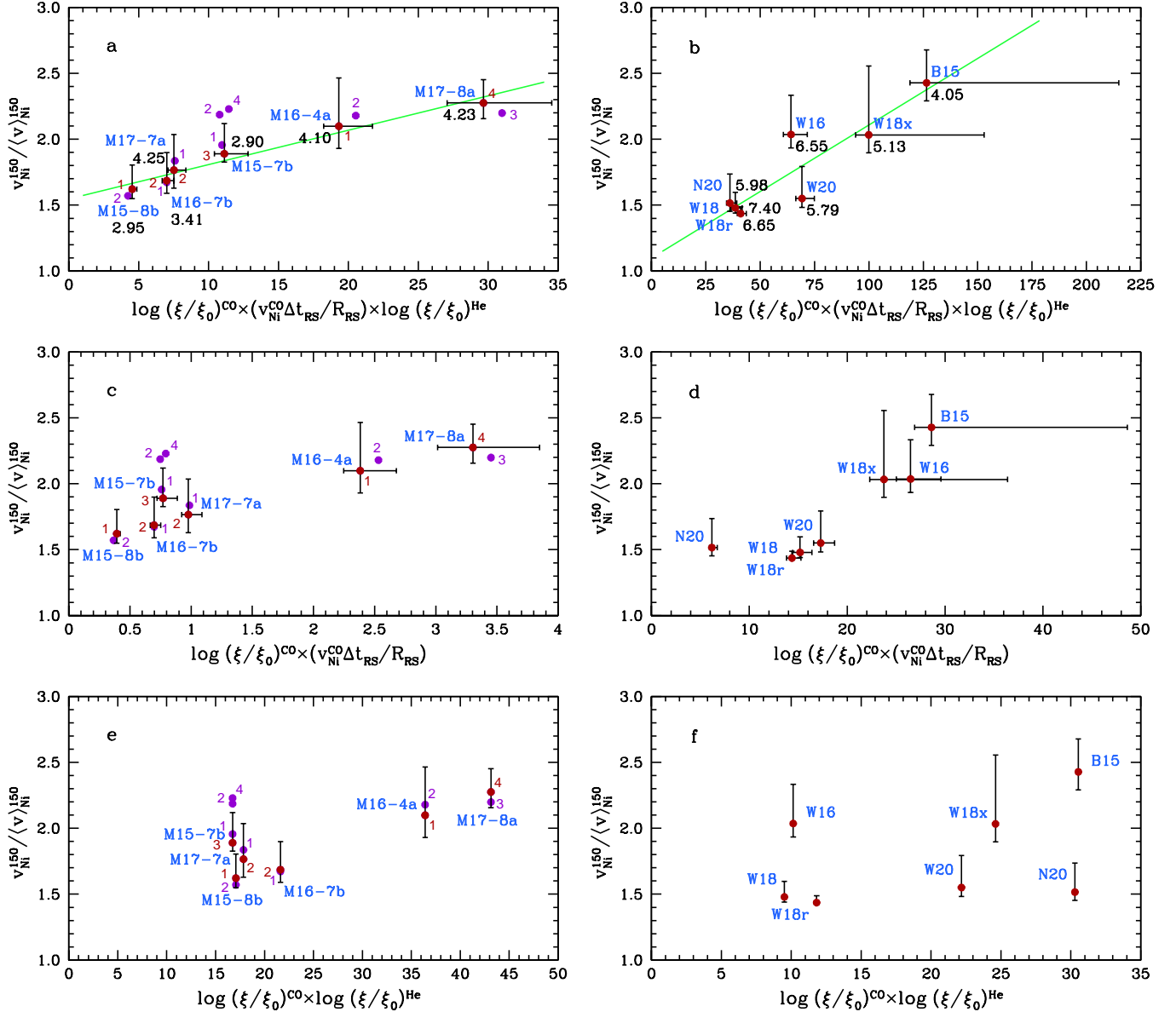


**Figure 10.** Dependence of the normalized extent of  $^{56}\text{Ni}$  mixing in velocity space on the hydrodynamic explosion properties linked to the structure of the binary-merger (left panels) and single-star (right panels) progenitors, listed in Table 3 and Table 3 in [Utrobin et al. \(2019\)](#), respectively. Names of the progenitor models are printed in blue. Numbers in black give the helium-core masses of the corresponding progenitor models. Red circles and figures show the reference models which explode with similar energies, and dark-violet circles and numbers for the binary-merger models represent the remaining models with different explosion energies. The uncertainties in the  $^{56}\text{Ni}$  mixing are estimated from estimates of the velocities of the  $^{56}\text{Ni}$  ejecta containing 93% and 99% of the total  $^{56}\text{Ni}$  mass. Green lines are least square fits which are based on the reference models. They prove a correlation between the extent of  $^{56}\text{Ni}$  mixing in velocity space and the hydrodynamic properties of the explosion models (for definitions of the quantities on the horizontal and vertical axis see the comments of Table 3).

the light curve. The total amount of radioactive  $^{56}\text{Ni}$  strongly affects the luminosity from about day 30 to the radioactive tail, and gives rise to the second dome-like maximum of the light curve of SN 1987A. While the total amount of  $^{56}\text{Ni}$  mainly determines the energy radiated during this period and the highest luminosity of the broad dome-like maximum, the amount of outward  $^{56}\text{Ni}$  mixing affects the smoothness of the rising part of the bolometric light curve just after the CRW

stage. The more extreme the large-scale mixing of  $^{56}\text{Ni}$  in velocity space is, the earlier the luminosity starts to grow to the dome-shaped maximum. The hydrodynamic models based on the pre-SN model M15-7b with maximum velocities of the bulk of ejected  $^{56}\text{Ni}$  equal to or exceeding about  $3000 \text{ km s}^{-1}$  (Table 2) most clearly demonstrate this dependence in comparison to the other hydrodynamic models (Figure 11). Along with the outward  $^{56}\text{Ni}$  mixing, hydrogen-rich



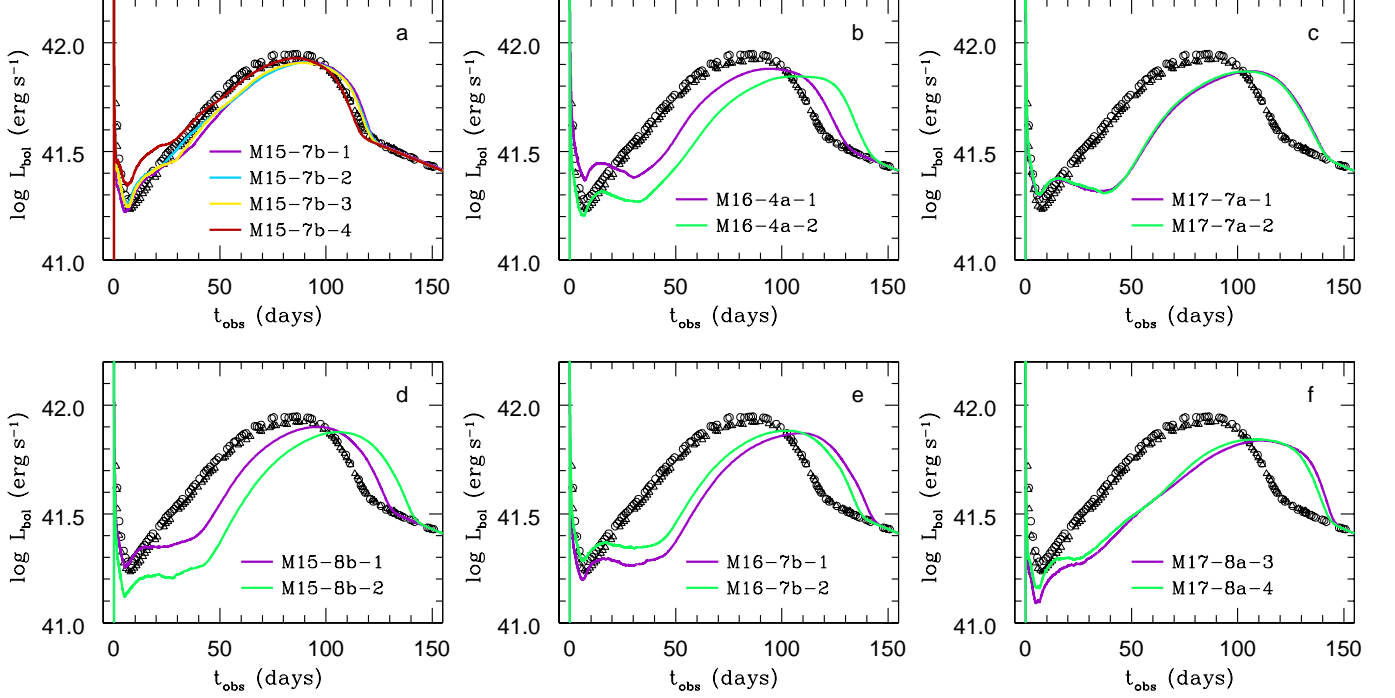


**Figure 11.** Bolometric light curves of hydrodynamic explosion models (Table 2) based on the pre-SN models M15-7b (a), M16-4a (b), M17-7a (c), M15-8b (d), M16-7b (e), and M17-8a (f) (Table 1). The computed light curves are compared with the observed bolometric luminosity of SN 1987A obtained by Catchpole et al. (1987, 1988) (open circles) and Hamuy et al. (1988) (open triangles).

matter is mixed down to the center. It increases the optical depth of the inner ejecta, because Thomson scattering off free electrons dominates the opacity of highly ionized matter. This, in turn, gives rise to a wide and luminous dome-shaped light-curve maximum (Figure 11).

For SN 1987A, the total amount of  $^{56}\text{Ni}$  in the ejecta is well fixed by the bolometric luminosity in the radioactive tail. Equating the observed bolometric luminosity in the radioactive tail to the gamma-ray luminosity gives a “directly observed” mass of radioactive  $^{56}\text{Ni}$  of  $0.0722 M_{\odot}$  with a distance modulus for the LMC of  $m - M = 18.5$  mag and a reddening of  $E(B - V) = 0.17$  mag (Utrobin et al. 2015). In all of our hydrodynamic models the initial  $^{56}\text{Ni}$  mass at the onset of light-curve modeling,  $M_{\text{Ni}}^i$ , is chosen such that the  $^{56}\text{Ni}$  mass in the ejecta evaluated at day 150,  $M_{\text{Ni}}^f$ , fits the observed luminosity in the radioactive tail. Taking fallback of  $^{56}\text{Ni}$  into account requires  $M_{\text{Ni}}^i$  to be greater than the value of  $M_{\text{Ni}}^f$ , which, in turn, exceeds the directly observed mass (Table 2) because of expansion-work effects (Utrobin 2007). The initial  $^{56}\text{Ni}$  masses of all 3D explosion models fall in between the minimum,  $M_{\text{Ni}}^{\min}$ , and maximum,  $M_{\text{Ni}}^{\max}$ , values listed in Table 2, and, consequently, these models are able to produce the amount of  $^{56}\text{Ni}$  that is needed to explain the SN 1987A observations.

### 3.7. Comparison with observations

For a comparison of our results of 3D hydrodynamic simulations of neutrino-driven explosions with observations of

SN 1987A, we consider the set of models M15-7b-3, M15-8b-1, M16-4a-1, M16-7b-2, M17-7a-2, and M17-8a-4 with comparable and SN 1987A-like explosion energies (Table 2). These hydrodynamic models are based on the corresponding compact blue binary-merger pre-SN models with radii of  $31.8 R_{\odot}$  to  $37.3 R_{\odot}$  (Table 1), which agree well with the photometric radius of the BSG Sanduleak  $-69^{\circ}202$  star of  $28.7 R_{\odot}$  to  $57.5 R_{\odot}$  (Arnett et al. 1989). Moreover, the pre-SN radii fall into the range of  $30 R_{\odot}$  to  $40 R_{\odot}$ , which is allowed by the hydrodynamic modeling and the time-dependent atmosphere model that explain both the bolometric light curve and the  $\text{H}\alpha$  profile of SN 1987A (Utrobin 2005). This and the fact that the outer layers of the pre-SN models have a suitable structure permit us to obtain a good reproduction of the initial luminosity peak within the first  $\sim 7$  days by all binary-merger models listed above (Figure 11). During the transition from the adiabatic cooling phase to the CRW phase a prominent minimum in the luminosity forms, which is observed at around day 7. All models of the subset compared here, except models M16-4a-1 and M17-8a-4, reproduce well the observed minimum (Figure 11). However, only one hydrodynamic model, M15-7b-3, also reproduces fairly well both the smooth rising part of the observed light curve and the major broad maximum with a duration of  $\sim 100$  days. The smoothness of the bolometric light curve of model M15-7b-3 results from the outward mixing of the bulk of radioactive  $^{56}\text{Ni}$  in velocity space up to  $2980 \text{ km s}^{-1}$  (Table 2), which is consistent with the observed value of about  $3000 \text{ km s}^{-1}$  (Colgan

et al. 1994), while all other models fall short of the required mixing.

The wide dome-like light curve maximum, in turn, arises from mixing a significant amount of hydrogen-rich matter down to the center. The analysis of the line profiles of hydrogen emission in the nebular phase (Chugai 1991; Kozma & Fransson 1998; Maguire et al. 2012), and the 3D view of H $\alpha$  emission (Larsson et al. 2016) and molecular hydrogen in SN 1987A (Larsson et al. 2019) show that hydrogen is mixed deeply down to velocities  $\leq 700 \text{ km s}^{-1}$ . It is noteworthy that in all hydrodynamic models hydrogen in the innermost layers of the ejecta expands with velocities lower than  $40 \text{ km s}^{-1}$  (Table 2), in good agreement with the observations. The mass of hydrogen confined to the inner layers ejected with velocities less than  $2000 \text{ km s}^{-1}$  may be considered as a measure of the optical depth of these layers, because hydrogen is the dominant contributor to opacity and the velocity at the photosphere observed in SN 1987A around the top of the dome-like maximum is about  $2000 \text{ km s}^{-1}$  (Phillips et al. 1988). It is the high optical depth of the inner ejecta that produces a wide and dome-shaped light-curve maximum. In model M15-7b-3 the hydrogen mass expanding with velocities less than  $2000 \text{ km s}^{-1}$  is  $3.1 M_{\odot}$  (Table 2), which is in good agreement with the observational constraint of  $2.2 M_{\odot}$  (Kozma & Fransson 1998).

The bolometric luminosity of SN 1987A in the radioactive tail can be formally fitted by the directly observed mass of radioactive  $^{56}\text{Ni}$  (see Section 3.6). In our case the required mass of  $^{56}\text{Ni}$  is  $0.0722 M_{\odot}$ , which is consistent within the errors with other empirical estimates of  $(0.069 \pm 0.003) M_{\odot}$  (Bouchet et al. 1991; McCray 1993) and  $(0.071 \pm 0.003) M_{\odot}$  (Seitenzahl et al. 2014). Unfortunately, the above observational numbers differ from the exact amount of radioactive  $^{56}\text{Ni}$  synthesized and ejected during an SN explosion. Even if there is no fallback of  $^{56}\text{Ni}$ , expansion-work effects definitely increase the  $^{56}\text{Ni}$  amount required in the hydrodynamic modeling to match the observed bolometric luminosity in the radioactive tail (compare the directly observed mass of  $0.0722 M_{\odot}$  with the values of  $M_{\text{Ni}}^f$  in Table 2). Moreover, both fallback of  $^{56}\text{Ni}$  and expansion-work effects make an assessment of the ejected  $^{56}\text{Ni}$  mass model-dependent.

Analyzing the evolution of the intensity and the profile of the oxygen doublet [O I]  $\lambda\lambda 6300, 6364 \text{ \AA}$  in the nebular phase showed that the mass of oxygen in SN 1987A is in the range from  $0.7 M_{\odot}$  to  $2.0 M_{\odot}$  (Li & McCray 1992; Chugai 1994; Chugai et al. 1997; Kozma & Fransson 1998; Jerkstrand et al. 2015). Our favorite model M15-7b-3 yields  $0.83 M_{\odot}$  (Table 2), which agrees with these observational constraints.

Kjær et al. (2010) and Larsson et al. (2013) studied the morphology of the ejecta using images and spectra in the emission lines of [Si I]+[Fe II] and He I, and in the emis-

sion lines of H $\alpha$  and [Si I]+[Fe II], respectively, and reconstructed the 3D shape of the inner regions of the ejecta. Kjær et al. (2010) approximated the actual 3D shape of the ejecta by an elongated triaxial ellipsoid. The 3D morphology of the observed emission lines reflects thermal and nonthermal emissivity produced, as a final result, by the energy deposition of gamma rays with energies of about 1 MeV from the decay chain  $^{56}\text{Ni} \rightarrow ^{56}\text{Co} \rightarrow ^{56}\text{Fe}$ . These gamma rays undergo Compton scattering by free and bound electrons in the ejecta, resulting in high-energy electrons which, in turn, deposit their energy by heating free electrons or by ionizing and exciting atoms and ions. The energy deposition and the ionization and excitation of individual elements are sensitive to the chemical composition. This fact and both gamma-ray and photon transport are responsible for hiding the details of the density distribution of the radioactive matter, but leave the possibility to trace at least its global properties. In other words, the observed emissivity distribution can provide valuable information about the spatial distribution of radioactive  $^{56}\text{Ni}$ . The 3D morphology of the  $^{56}\text{Ni}$ -rich ejecta in the model sequence M17-8a-4, M16-4a-1, M15-7b-3, M17-7a-2, M16-7b-2, and M15-8b-1 long after shock breakout gradually changes from a practically one-sided, dipolar configuration to an almost basically spherical one with a dominant monopole (Figure 5, second and fourth columns). Among these models only our favorite model M15-7b-3 has a distribution of  $^{56}\text{Ni}$ -rich matter in velocity space with a strong dipole component, which resembles the elongated ellipsoid inferred from observations better than any other model.

#### 4. CONSTRAINING THE PROGENITOR MASS

Alp et al. (2019) showed that our favorite model M15-7b-3 having an ejecta mass of  $19.46 M_{\odot}$  fits the early X-ray and gamma-ray emission of SN 1987A best compared to other binary-merger explosion models. Jerkstrand et al. (2020), in turn, found that a good agreement between 3D models and the gamma-ray decay lines and the UVOIR bolometric light curve of SN 1987A could be achieved with a lower ejecta mass of about  $14 M_{\odot}$ . In the light of these results we computed a set of artificial models M15-7b-3-m2, M15-7b-3-m4, and M15-7b-3-m6 with ejecta masses of  $17.46 M_{\odot}$ ,  $15.46 M_{\odot}$ , and  $13.46 M_{\odot}$ , respectively (Table 4). To realize the reduction of the ejecta mass, we decreased the density by the corresponding factor in each mass zone. This simple approach preserves both the shape of the profiles of density and all species in velocity space (i.e. the extent of hydrogen and nickel mixing), and the ratio of explosion energy and ejecta mass. Thereby the structure of the helium core becomes incompatible with that of the evolutionary model, but this is the price to pay for the simplicity of the approach. The total  $^{56}\text{Ni}$  mass for the auxiliary hydrodynamic models is fitted to the

**Table 4.** Basic properties of auxiliary hydrodynamic models

Model	$M_{\text{ej}}$ ( $M_{\odot}$ )	$E_{\text{exp}}$ (B)	$M_{\text{Ni}}^f$ ( $10^{-2} M_{\odot}$ )	$\Delta M_{\text{H}}^{2000}$ ( $M_{\odot}$ )
M15-7b-3	19.46	1.432	7.28	3.10
M15-7b-3-m2	17.46	1.289	7.28	2.76
M15-7b-3-m4	15.46	1.146	7.28	2.41
M15-7b-3-m6	13.46	1.001	7.28	2.07

NOTE—The auxiliary models are based on the pre-SN model M15-7b (Table 1) and the explosion model M15-7b-3 (Table 2).  $M_{\text{ej}}$  is the ejecta mass;  $E_{\text{exp}}$  the explosion energy;  $M_{\text{Ni}}^f$  the  $^{56}\text{Ni}$  mass ejected at day 150;  $\Delta M_{\text{H}}^{2000}$  the mass of hydrogen confined to the inner layers ejected with velocities less than  $2000 \text{ km s}^{-1}$ .

luminosity in the radioactive tail in the same way as in the case of the 3D explosion models.

The corresponding light curves are depicted in Figure 12(a). The original model M15-7b-3 shows a good overall agreement with the observed light curve even though the dome of the calculated light curve should be slightly shifted as a whole to earlier times. The latter effect is easily realized by decreasing the mass of the ejected envelope (Utrobin 2005), which is in perfect agreement with the analysis of X-ray and gamma-ray observations, and Fe IR line properties of SN 1987A by Jerkstrand et al. (2020). Decreasing the ejecta mass and, as a consequence, the mass of slow-moving hydrogen confined to the inner layers (Table 4) shifts both the rising part of the dome-like maximum of the light curve and the branch declining from the maximum to the radioactive tail to earlier times. The former is due to a shortening of the diffusion time, which is linked to the reduction of the total optical depth of the envelope. The latter effect is due to a decrease of the total radiation energy of the ejecta, which is clearly demonstrated in Figure 12(b). We ignore the total internal gas energy of the ejecta because it is negligible compared to that of radiation (Utrobin 2007). Note that the time-integrated energy deposition by radioactive decays does not change with varied ejecta mass because the envelope remains optically thick for gamma rays. Also the time-integrated emergent energy is almost independent of the ejecta mass (Figure 12(b)).

Varying the ejecta mass of models M15-7b-3, M15-7b-3-m2, M15-7b-3-m4, and M15-7b-3-m6 from  $19.46 M_{\odot}$  to  $13.46 M_{\odot}$  reveals that the light curves of models M15-7b-3-m2 and M15-7b-3-m4 agree better with the dome-like maximum of the observed light curve than the original model M15-7b-3, whereas model M15-7b-3-m6 shows a noticeable deficit in the luminosity during the transition from the max-

imum to the radioactive tail (Figure 12(a)). This luminosity deficit in model M15-7b-3-m6 is connected to a deficit in the radiated energy, which, in turn, is related to the lower total radiation energy of the ejecta compared to that of other models under consideration (Figure 12(b)). The seemingly small deficit of the total radiation energy in model M15-7b-3-m6 during the transition from the maximum to the radioactive tail turns out to be fairly significant because of a lack of other sources of energy except for a little remaining energy deposition by radioactive decays. This fact is of great importance and allows us to discard model M15-7b-3-m6 from our consideration because it is less consistent with the observations of SN 1987A and has a severe deficiency in the energy budget during the transition from the broad maximum to the radioactive tail.

The experiment undertaken here demonstrates convincingly that a hydrodynamic model based on model M15-7b-3 with a lower ejecta mass in the range of  $17.46 M_{\odot}$  to  $15.46 M_{\odot}$  allows for a better agreement with the observations, confirming the conclusions of Jerkstrand et al. (2020). Of course, an open question arises, whether a lower explosion energy (Table 4) would allow for sufficiently strong mixing and a sufficiently high maximum velocity of the bulk mass of  $^{56}\text{Ni}$  consistent with observations of SN 1987A.

## 5. COMPARISON BETWEEN SINGLE-STAR AND BINARY-MERGER MODELS

The study undertaken in this paper in the framework of the neutrino-driven explosion mechanism provides a unique opportunity to compare single-star and binary-merger progenitor models in reproducing the observed properties of the BSG Sanduleak –69°202 star and the SN 1987A explosion. To carry out a comparative analysis of the single-star and binary-merger models, we briefly summarize the key observational constraints for SN 1987A:

1. The pre-SN star, Sanduleak –69°202, was a blue B3 Ia supergiant (Rousseau et al. 1978; Gilmozzi et al. 1987; Walborn et al. 1987; Sonneborn et al. 1987) whose location in the HRD is determined by an effective temperature of 14 000 K to 17 000 K (Humphreys & McElroy 1984; Trundle et al. 2004; Crowther et al. 2006; Searle et al. 2008) and a luminosity of  $(3 - 6) \times 10^3 \text{ erg s}^{-1}$  (Arnett et al. 1989).
2. The directly observed mass of radioactive  $^{56}\text{Ni}$  deduced from a formal fit to the actual bolometric luminosity in the radioactive tail is equal to  $0.0722 M_{\odot}$  (Utrobin et al. 2015), which is consistent within the errors with other empirical estimates of  $(0.069 \pm 0.003) M_{\odot}$  (Bouchet et al. 1991; McCray 1993) and  $(0.071 \pm 0.003) M_{\odot}$  (Seitenzahl et al. 2014).

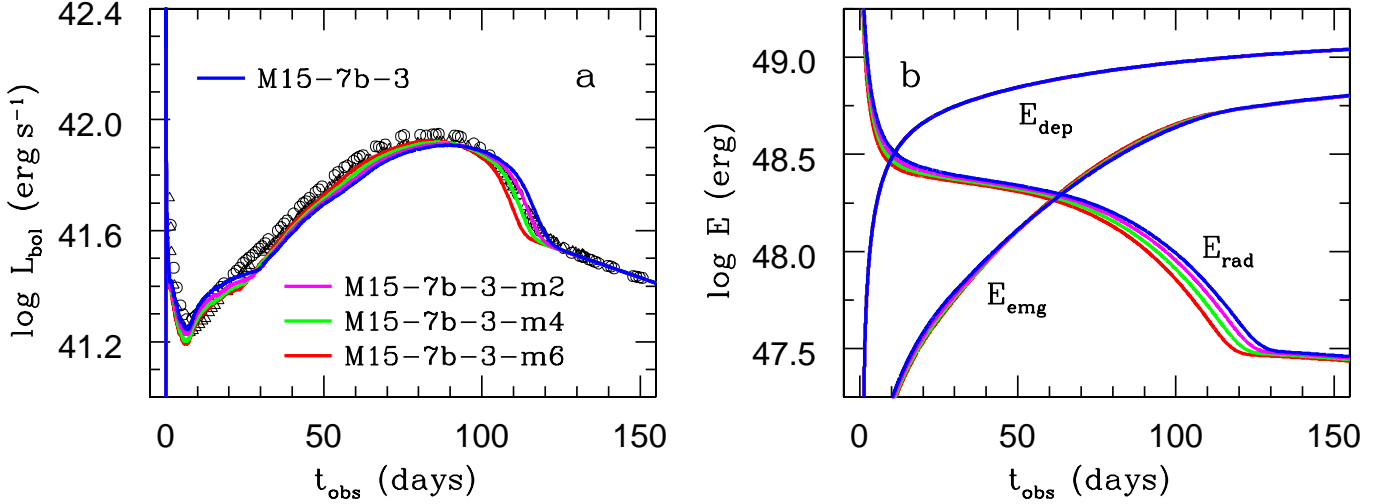


**Figure 12.** Dependence on the ejecta mass. Bolometric light curves (a) and time-integrated energy deposition by radioactive decays,  $E_{\text{dep}}$ , time-integrated emergent energy,  $E_{\text{emg}}$ , and total radiation energy of the ejecta,  $E_{\text{rad}}$ , as a function of time (b) for models M15-7b-3 ( $M_{\text{ej}} = 19.46 M_{\odot}$ ), M15-7b-3-m2 ( $17.46 M_{\odot}$ ), M15-7b-3-m4 ( $15.46 M_{\odot}$ ), and M15-7b-3-m6 ( $13.46 M_{\odot}$ ). The computed light curves are compared with the observed bolometric luminosity of SN 1987A obtained by Catchpole et al. (1987, 1988) (open circles) and Hamuy et al. (1988) (open triangles).

**Table 5.** Subset of the best explosion models of single-star and binary-merger progenitors

Model	$M_{\text{NS}}$	$M_{\text{CO}}^{\text{core}}$	$M_{\text{He}}^{\text{core}}$	$M_{\text{ej}}$	$R_{\text{pSN}}$	$E_{\text{exp}}$	$M_{\text{Ni}}^{\text{f}}$	$v_{\text{Ni}}^{\text{bulk}}$	$v_{\text{H}}^{\text{min}}$	$\Delta M_{\text{H}}^{2000}$	$M_{\text{O}}$	Remark
		$(M_{\odot})$			$(R_{\odot})$	$(\text{B})$	$(10^{-2} M_{\odot})$	$(\text{km s}^{-1})$		$(M_{\odot})$		
B15-2	1.25	1.64	4.05	14.20	56.1	1.40	7.25	3370	28	0.922	0.16	single-star
W18x-2	1.52	2.12	5.13	16.03	30.4	1.45	7.55	2460	147	0.847	0.36	single-star
M15-7b-3	1.58	2.48	2.90	19.46	37.0	1.43	7.28	2980	29	3.10	0.83	binary-merger
M15-8b-1	1.32	2.50	2.95	20.73	31.8	1.57	7.40	1829	27	3.14	0.96	binary-merger
Constraint					28.7–57.5		$\approx 7.22$	$\sim 3000$	$\leq 700$	$\sim 2.2$	0.7–2.0	

- The analysis of the infrared emission lines of [Ni II] and [Fe II] in the nebular phase shows that the bulk of the radioactive  $^{56}\text{Ni}$  was moving with a maximum velocity of  $\sim 3000 \text{ km s}^{-1}$  (Colgan et al. 1994).
- The line profiles of the hydrogen emission in the nebular phase (Chugai 1991; Kozma & Fransson 1998; Maguire et al. 2012), and the 3D geometry of the  $\text{H}\alpha$  emission (Larsson et al. 2016) and of molecular hydrogen (Larsson et al. 2019) showed that hydrogen-rich matter is mixed deeply down to velocities  $\leq 700 \text{ km s}^{-1}$ .
- Kozma & Fransson (1998) constrained quantitatively the mass of hydrogen-rich matter that expanded with velocities lower than  $2000 \text{ km s}^{-1}$  to about  $2.2 M_{\odot}$ .
- The observed bolometric light curve has a prominent, broad maximum of dome-like shape (Catchpole et al. 1987, 1988; Hamuy et al. 1988).
- The overall shape of the bolometric light curve, which is characterized by a narrow initial luminosity peak during the first  $\sim 7$  days and the broad dome-like maximum with a characteristic width of  $\sim 100$  days (Catchpole et al. 1987, 1988; Hamuy et al. 1988), is a specific feature of the peculiar Type IIP SN 1987A in contrast to ordinary Type IIP SNe.
- The kinematics of the ejected envelope is well deduced from the evolution of the photospheric velocity, which was estimated by Phillips et al. (1988) using the absorption minimum of the Fe II 5169 Å line.
- The mass of oxygen in the SN ejecta is in the range of  $0.7 M_{\odot}$  to  $2.0 M_{\odot}$  (Li & McCray 1992; Chugai 1994; Chugai et al. 1997; Kozma & Fransson 1998; Jerkstrand et al. 2015).
- Kjær et al. (2010) and Larsson et al. (2013) studied spectra and images in the emission lines of



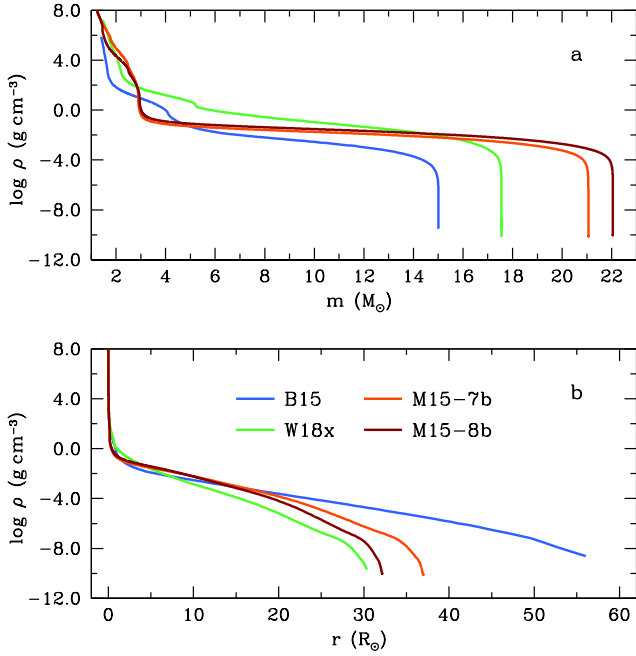


**Figure 13.** Density profiles as function of interior mass (a) and as function of radius for the whole star (b) in the single-star pre-SN models B15 and W18x (Utrobin et al. 2019), and in the binary-merger pre-SN models M15-7b and M15-8b (Table 1).

[Si I]+[Fe II] and He I and in the emission lines of H $\alpha$  and [Si I]+[Fe II], respectively, and reconstructed the 3D shape of the inner regions of the ejecta. Kjær et al. approximated the actual 3D shape by an elongated triaxial ellipsoid.

11. The hard X-ray and gamma-ray emission is very sensitive to macroscopic mixing in the SN ejecta, the ejecta structure, and the ejecta mass. Alp et al. (2019) analyzed the early hard X-ray and gamma-ray observations of SN 1987A to test 3D hydrodynamic simulations of neutrino-driven explosions.
12. Using 3D hydrodynamic simulations of neutrino-driven explosions, Jerkstrand et al. (2020) studied the gamma-ray decay lines and the UVOIR bolometric light curve of SN 1987A to deduce constraints on the asymmetry of radioactive ejecta and the ejected envelope mass.

To quantify the quality of single-star and binary-merger explosion models, we compare the best and second-best model based on the agreement between simulations and observations using wide range of criteria. Hydrodynamic simulations of single stars resulted in the best and second-best model being models B15-2 and W18x-2 (Utrobin et al. 2019), while our simulations of binary mergers yield M15-7b-3 and M15-8b-1 as the best and second-best model, respectively. These models constitute the subset of our best

single-star and binary-merger explosion models, whose basic properties are listed in Table 5. The structure of their progenitor models are depicted in Figure 13, the bolometric light curves in Figure 14(a), and the evolution of the photospheric velocity in Figure 14(b). This subset of models allows us not only to estimate how well the selected models match the observations, but also to demonstrate differences between the best and second-best model.

Comparing the models in the subset, in the framework of neutrino-driven explosions, we obtain the following results:

1. Sukhbold et al. (2016) clearly demonstrated that the single-star progenitor model B15 (W15 in the nomenclature of Sukhbold et al.) has a helium-core mass and a luminosity that are both too small compared to the observational constraints imposed by the location of the Sanduleak  $-69^{\circ}202$  star in the HRD, whereas model W18x agrees well with these constraints. All of the binary-merger progenitor models provided by Menon & Heger (2017) for this study are located in or close to the region of the observed properties of Sanduleak  $-69^{\circ}202$  in the HRD.
2. The 3D neutrino-driven explosion simulations of both the single-star models B15-2 and W18x-2 and the binary-merger models M15-7b-3 and M15-8b-1 are capable of producing the initial (at the onset of light-curve modeling)  $^{56}\text{Ni}$  masses required to match the observations of the radioactive tail of SN 1987A (Table 5).
3. Both of the two best models, B15-2 and M15-7b-3, yield a maximum velocity of the bulk of  $^{56}\text{Ni}$  consistent with the observed value of about  $3000 \text{ km s}^{-1}$  in contrast to the second-best models, W18x-2 and M15-8b-1, which do not fulfill this constraint of SN 1987A (Table 5).
4. In the single-star and binary-merger models considered here the inward mixing of hydrogen, occurring during the 3D neutrino-driven simulations, results in minimum velocities of hydrogen-rich matter of less than  $150 \text{ km s}^{-1}$  (Table 5), which is in good agreement with the spectral observations of SN 1987A.
5. Table 5 shows that the single-star models B15-2 and W18x-2 contain masses of hydrogen-rich matter expanding with velocities lower than  $2000 \text{ km s}^{-1}$  that are a factor of two lower than the observational constraint of about  $2.2 M_{\odot}$ , whereas the binary-merger models M15-7b-3 and M15-8b-1 even exceed it.
6. For the binary-merger models M15-7b-3 and M15-8b-1 the broad domes of the calculated light curves are very similar in shape to the observed one, but they

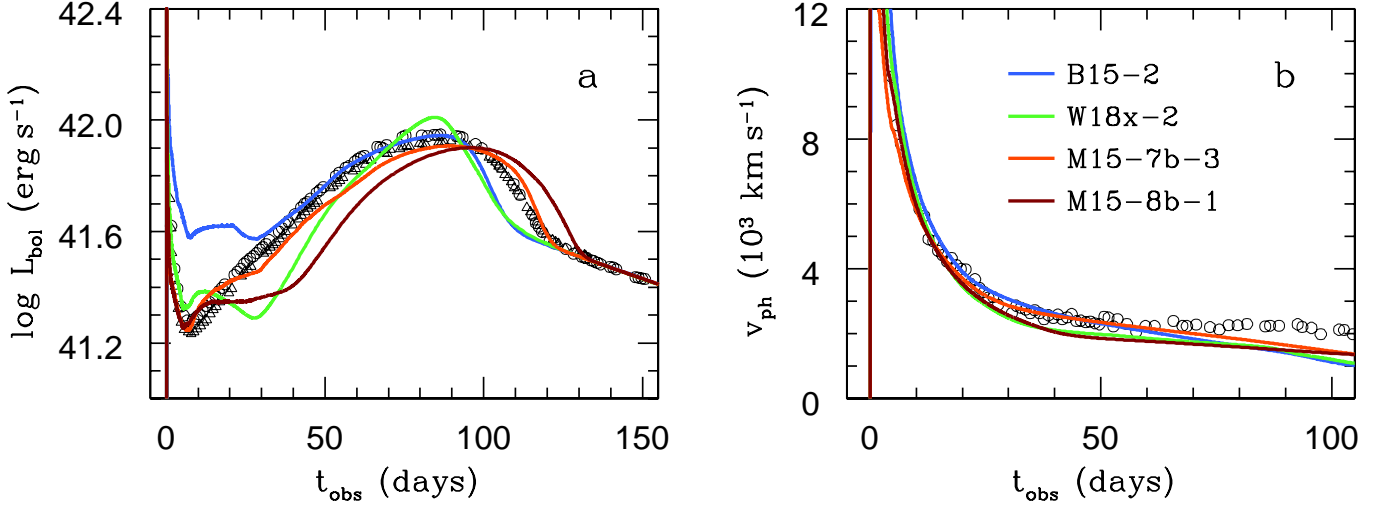


**Figure 14.** Bolometric light curves (a) and photospheric velocity (b) as function of time for models B15-2, W18x-2, M15-7b-3, and M15-8b-1. We define the photosphere to be the spherical surface at which the Thomson optical depth is  $2/3$ . The computed results are compared with the observed bolometric luminosity of SN 1987A obtained by [Catchpole et al. \(1987, 1988\)](#) (open circles) and [Hamuy et al. \(1988\)](#) (open triangles), and with the velocity at the photosphere estimated by [Phillips et al. \(1988\)](#) with the absorption minimum of the Fe II 5169 Å line (open circles).

**Table 6.** Comparative analysis of single-star and binary-merger models

Observational constraint	Single-star	Binary-merger
	B15-2 / W18x-2	M15-7b-3 / M15-8b-1
1. location of Sanduleak –69°202 in the HRD	– / +	+ / +
2. production of $^{56}\text{Ni}$ in 3D simulations	+ / +	+ / +
3. maximum velocity of the bulk of $^{56}\text{Ni}$	+ / –	+ / –
4. minimum velocity of hydrogen matter	+ / +	+ / +
5. mass of hydrogen with $v < 2000 \text{ km s}^{-1}$	– / –	+ / +
6. dome shape of the light curve	+ / –	+ / +
7. global shape of the light curve	– / –	+ / –
8. evolution of the photospheric velocity	+ / –	+ / –
9. oxygen mass in the SN ejecta	– / –	+ / +
10. 3D shape of the $^{56}\text{Ni}$ ejecta	– / +	+ / –
11. X-ray and gamma-ray emission	+ /	+ / –
12. gamma-ray decay lines	+ / –	– / –
Total score	7 : 12 / 4 : 11	11 : 12 / 6 : 12

are slightly less luminous and shifted to a slightly later epoch (Figure 14(a)). In contrast, the dome of the single-star model B15-2 satisfactorily fits the observed one, while the dome of model W18x-2 displays a peaked shape and disagrees with the observations. The quality of the dome-shape fits partially correlates with the mass of hydrogen-rich matter mixed inward to a velocity of  $\lesssim 2000 \text{ km s}^{-1}$  and the mass of the ejecta (Table 5).

7. The binary-merger model M15-7b-3 matches the overall shape of the observed bolometric light curve much better than any of the other models (Figure 14(a)). The narrow initial luminosity peak during the first  $\sim 7$  days results from a relatively small radius of the corresponding pre-SN model of  $37.0 R_{\odot}$  (Table 5) and a suitable structure of its outer layers (Figure 13). A combination of the maximum velocity of the bulk mass of  $^{56}\text{Ni}$  around  $3000 \text{ km s}^{-1}$  and the mass of hydrogen-rich matter of  $3.10 M_{\odot}$  mixed inward to a velocity of  $\lesssim 2000 \text{ km s}^{-1}$  (Table 5) produces the smooth and

monotonic rising part of the light curve and its broad dome-like maximum with a characteristic width of  $\sim 100$  days.

8. The evolution of the photospheric velocity of both best models B15-2 and M15-7b-3 is in good agreement with that observed during the first 60 days when the position of the photosphere is more or less correctly determined in the light-curve simulations, whereas the agreement is worse for the other two models (Figure 14(b)). After the photospheric velocity has decreased below  $3000 \text{ km s}^{-1}$ , which is the maximum speed of the bulk mass of the  $^{56}\text{Ni}$ -rich matter, around day 30, the asymmetry in the 3D morphology of the inner regions of the ejecta studied by Kjær et al. (2010) and Larsson et al. (2013) can gradually affect the shape of the photosphere. The disparity between the calculated and observed photospheric velocities after about 60 days most likely stems from assuming a spherical  $^{56}\text{Ni}$  distribution in our 1D simulations.
9. The mass of oxygen in the ejecta of the binary-merger models M15-7b-3 and M15-8b-1 falls in the observed range of  $0.7 M_{\odot}$  to  $2.0 M_{\odot}$ , but the single-star models B15-2 and W18x-2 have oxygen masses significantly below this range (Table 5).
10. The 3D morphology of the  $^{56}\text{Ni}$ -rich ejecta in the binary-merger model M15-7b-3 long after shock breakout has a pronounced dipole component (Figure 5, upper row, second column), which resembles well the elongated-ellipsoid shape that was extracted from spectra and images of SN 1987A in the emission lines in the nebular phase. Except for a single prominent clump moving with a velocity of about  $3000 \text{ km s}^{-1}$ , the 3D explosion morphology of the single-star model W18x-2 is of approximately elongated ellipsoidal shape (Utrobin et al. 2019, Figure 4, lower row, last column). The two other models of M15-8b-1 (Figure 5, upper row, last column) and B15-2 (Utrobin et al. 2019, Figure 4, lower row, first column) have a morphology that is closer to a spherical shape than to an elongated ellipsoid.
11. Alp et al. (2019) computed the early hard X-ray and gamma-ray emission produced by 3D neutrino-driven explosion models of single-star and binary-merger progenitors, and compared the emergent emission with the corresponding spectra, continuum light curves, and line fluxes of SN 1987A. They showed that the single-star model B15-2 and the binary-merger model M15-7b-3 are basically consistent with the X-ray and gamma-ray observations, whereas model M15-8b-1

fails to match them. Model W18x-2 is not investigated in that study.

12. Analyzing the gamma-ray decay lines and the UVOIR bolometric light curve of SN 1987A up to 600 days, Jerkstrand et al. (2020) found that the 3D explosion models show good agreement with the observations only for an ejecta mass of about  $14 M_{\odot}$  and a kinetic energy of around  $1.5 \times 10^{51} \text{ erg}$ . It is important that our auxiliary hydrodynamic models based on model M15-7b-3 and having an ejecta mass in the range of  $17.46 M_{\odot}$  to  $15.46 M_{\odot}$ , i.e., lower than in the reference model M15-7b-3, result in a better agreement with the photometric observations of SN 1987A (see Section 4).

For a concise presentation of the results of the above comparative analysis and their adequate assessment, we list all twelve observational constraints in Table 6, where plus signs stand for matching the constraint, minus signs for not matching, and a blank space for a lack of the relevant data. Assuming equal weights for all constraints of the analysis, we conclude that our favorite binary-merger explosion model M15-7b-3 matches all of the constraints except for point No. 12, demonstrating an overwhelming superiority over the other models. Only point 12 still poses a problem, because the ejecta mass of the explosion model M15-7b-3 is too large. This points to a shortcoming of the binary-merger progenitor model M15-7b, whose pre-collapse mass is too high to avoid this problem. Among the single-star explosions, model B15-2 has some important favorable properties – namely the maximum velocity of the bulk of  $^{56}\text{Ni}$ , the dome of the light curve, and the X-ray and gamma-ray emission – that agree with observations.

Note that Ono et al. (2020) compared 3D single-star and binary-merger explosions by their ability to reproduce the observed infrared emission lines of [Fe II] (Haas et al. 1990) and to satisfy the constraint imposed by the fast  $^{56}\text{Ni}$  clump (Utrobin et al. 1995). Their 3D explosion modeling was not self-consistent (because they imposed the explosion asymmetry by hand), but in line with our conclusions, they independently found that the explosion of the binary-merger progenitor model, which was initiated by an asymmetric bipolar-like SN shock, reproduces the observations better than the single-star explosion.

## 6. CONCLUSIONS

In this work we compare the results of 3D neutrino-driven explosion simulations and light curve modeling, based on progenitor models of Sanduleak –69°202 evolved in a binary-merger scenario with the observations of the peculiar Type IIP SN 1987A. We draw the following conclusions:

- The radii of the compact blue binary-merger progenitor models are in between  $31.8 R_{\odot}$  and  $37.3 R_{\odot}$  (Ta-

- ble 1) and agree well with the photometric radius of the BSG Sanduleak  $-69^{\circ}202$  star of  $28.7 R_{\odot}$  to  $57.5 R_{\odot}$  (Arnett et al. 1989). In addition, these pre-SN radii are in agreement with those of  $30 R_{\odot}$  to  $40 R_{\odot}$  allowed by hydrodynamic explosion modeling and a time-dependent atmosphere model that explain the photometric and spectroscopic observations of SN 1987A (Utrobin 2005). Such pre-SN radii and the structure of the outer layers are suitable to reproduce the observed initial luminosity peak during the first  $\sim 7$  days (Figure 11) with explosions of all of our binary-merger models M15-7b-3, M15-8b-1, M16-4a-1, M16-7b-2, M17-7a-2, and M17-8a-4, which have comparable and SN 1987A-like explosion energies (Table 2).
- After the first 20 days, we see some non-monotonic behavior (and partly short-timescale variability) in the light curves of all of the explosion models instead of the smooth and monotonic behavior of the observed light curve (Figure 11). The rising part of the light curve depends both on the structure of the pre-SN model (Utrobin 2004) and on the extent of outward mixing of radioactive  $^{56}\text{Ni}$  (Utrobin 2004; Utrobin et al. 2019, Figure 8). Strong outward mixing of  $^{56}\text{Ni}$  in models M15-7b-1, M15-7b-2, M15-7b-3, and M16-4a-1 (Table 2) – which exceeds the observational constraint on the maximum velocity for the bulk mass of  $^{56}\text{Ni}$  of about  $3000 \text{ km s}^{-1}$  – produces an almost smooth and monotonic rising part of the calculated light curves. In contrast, weaker mixing of  $^{56}\text{Ni}$  in some of the explosion models results in non-smooth and non-monotonic behavior.
  - The domes of all calculated light curves are very similar in shape to the observed behavior, but they are less luminous and shifted to a later epoch (Figure 11). For the 3D explosion models based on progenitor M15-7b both of these shortcomings are small, however. This effect is explained by a larger optical depth of the inner layers than in the single-star explosion model B15-2, whose dome of the light curve agrees with the observations of SN 1987A much better than that of all other single-star explosion models (Utrobin et al. 2015, Figure 11). The higher optical depth in the binary-merger explosion models is caused by a much higher abundance of hydrogen in the inner layers. The last fact is evident from the mass of hydrogen mixed into the helium shell, which is about  $0.5 M_{\odot}$  in the explosion models of our binary-merger progenitors (Table 2) compared to  $0.15 M_{\odot}$  in model B15-2 (Utrobin et al. 2019, Table 2).
  - The initial  $^{56}\text{Ni}$  mass (at the time of shock breakout) required to match the observations of SN 1987A in the

radioactive tail (Figure 11) is below the maximum production of  $^{56}\text{Ni}$  estimated for all of our 3D explosion models (Table 2). Thus, the 3D neutrino-driven explosion simulations considered in this study are able to synthesize the ejected amount of radioactive  $^{56}\text{Ni}$ .

- The sequence of the binary-merger explosion models M15-7b-3, M15-8b-1, M16-4a-1, M16-7b-2, M17-7a-2, and M17-8a-4, all of which have nearly the same and SN 1987A-like explosion energies, showed, similar to the single-star models, that the extent of outward radioactive  $^{56}\text{Ni}$  mixing in the framework of the 3D neutrino-driven simulations depends mainly on the following three explosion-related properties, which depend on the structure of the progenitor models: high growth factors of RT instabilities at the (C+O)/He and He/H composition interfaces, and a weak interaction of fast RT plumes with the reverse shock occurring below the He/H composition interface. An optimal combination of these three factors turned out to be a sufficient condition for efficient outward mixing of  $^{56}\text{Ni}$  into the hydrogen envelope.
- Kozma & Fransson (1998) quantitatively constrained the mass of hydrogen-rich gas mixed to velocities of  $\lesssim 2000 \text{ km s}^{-1}$  to about  $2.2 M_{\odot}$ . Models M15-7b-4 and M16-4a-1 agree well with this observational constraint, whereas other models yield significantly higher masses of hydrogen matter in the range of  $3.07 M_{\odot}$  to  $6.41 M_{\odot}$  mixed below  $2000 \text{ km s}^{-1}$  (Table 2).
- The masses of oxygen in the ejecta of the binary-merger models fall in the range of  $0.83 M_{\odot}$  to  $1.29 M_{\odot}$  (Table 2) and are fully consistent with the observed range of  $0.7 M_{\odot}$  to  $2.0 M_{\odot}$  (Li & McCray 1992; Chugai 1994; Chugai et al. 1997; Kozma & Fransson 1998; Jerkstrand et al. 2015).
- Analyzing the gamma-ray decay lines and the UVOIR bolometric light curve of SN 1987A, Jerkstrand et al. (2020) find that 3D neutrino-driven explosion simulations show good agreement with the observations only for an ejecta mass of about  $14 M_{\odot}$  and a kinetic energy of around  $1.5 \times 10^{51} \text{ erg}$ . Being aware of this result, we computed auxiliary explosion models based on model M15-7b-3, which had an ejecta mass in the range of  $17.46 M_{\odot}$  to  $15.46 M_{\odot}$ , which is lower than in the reference model M15-7b-3. These models show a better agreement with the photometric observations than the reference model (Section 4).
- A comparative analysis of 3D neutrino-driven explosion simulations and light curve modeling of SN 1987A (Section 5) based on progenitors evolved



in both single-star and binary-merger scenarios shows that only binary-merger model M15-7b-3 matches eleven of twelve crucial observational constraints, including the observational properties of the BSG Sanduleak  $-69^{\circ}202$  star, demonstrating a remarkable superiority compared to other single-star and binary-merger models (Table 6). Among the single-star models, model B15-2 has some favorable properties – namely the maximum velocity of the bulk of  $^{56}\text{Ni}$ , the dome of the light curve, and the X-ray and gamma-ray emission – that agree with observations.

As in [Utrobin et al. \(2015, 2019\)](#), we did not fine-tune the modeling approach for SN 1987A, except for choosing a suitable explosion energy, to achieve good agreement of the 3D neutrino-driven explosion models and the corresponding light-curve results with observations of SN 1987A.

Our results are a promising step forward towards fully self-consistent models that can explain the observed properties of SN 1987A. They provide strong support to the binary-merger scenario for the BSG progenitor star of this supernova. Moreover, they permit the expectation that further progress will be achieved by improved binary-merger progenitor models, having a smaller pre-collapse mass, higher resolution 3D explosion simulations to later evolution stages beyond the decay time of  $^{56}\text{Ni}$  and  $^{56}\text{Co}$  ([Gabler et al. 2021](#)), and a treat-

ment of radiative transfer including 3D effects (e.g., [Dessart & Audit 2019](#)).

## ACKNOWLEDGMENTS

V.P.U. was supported by the guest program of the Max-Planck-Institut für Astrophysik and by Russian Scientific Foundation grant 19-12-00229 in his work on radiation-hydrodynamics simulations for supernova light-curve modeling with the code CRAB. A.H. was supported by the Australian Research Council (ARC) Centre of Excellence (CoE) for Gravitational Wave Discovery (OzGrav) project number CE170100004 and by the ARC CoE for All Sky Astrophysics in 3 Dimensions (ASTRO 3D) project number CE170100013. A.H.’s contribution benefited from support, in part, by the National Science Foundation under Grant No. PHY-1430152 (JINA Center for the Evolution of the Elements). At Garching, funding by the Deutsche Forschungsgemeinschaft (DFG, German Research Foundation) through Sonderforschungsbereich (Collaborative Research Center) SFB-1258 “Neutrinos and Dark Matter in Astro- and Particle Physics (NDM)” and under Germany’s Excellence Strategy through Cluster of Excellence ORIGINS (EXC-2094)–390783311, and by the European Research Council through Grant ERC-AdG No. 341157-COCO2CASA is acknowledged. Computation of the 3D models and postprocessing of the data were done on Hydra of the Rechenzentrum Garching.

## REFERENCES

- Alp, D., Larsson, J., Maeda, K., et al. 2019, *ApJ*, 882, 22, doi: [10.3847/1538-4357/ab3395](#)
- Arcones, A., Janka, H.-T., & Scheck, L. 2007, *A&A*, 467, 1227, doi: [10.1051/0004-6361:20066983](#)
- Arnett, W. D. 1987, *ApJ*, 319, 136, doi: [10.1086/165439](#)
- Arnett, W. D., Bahcall, J. N., Kirshner, R. P., & Woosley, S. E. 1989, *ARA&A*, 27, 629, doi: [10.1146/annurev.aa.27.090189.003213](#)
- Asplund, M., Grevesse, N., Sauval, A. J., & Scott, P. 2009, *ARA&A*, 47, 481, doi: [10.1146/annurev.astro.46.060407.145222](#)
- Bouchet, P., Phillips, M. M., Suntzeff, N. B., et al. 1991, *A&A*, 245, 490
- Castor, J. I., Abbott, D. C., & Klein, R. I. 1975, *ApJ*, 195, 157, doi: [10.1086/153315](#)
- Catchpole, R. M., Menzies, J. W., Monk, A. S., et al. 1987, *MNRAS*, 229, 15P
- Catchpole, R. M., Whitelock, P. A., Feast, M. W., et al. 1988, *MNRAS*, 231, 75P
- Catchpole, R. M., Whitelock, P. A., Menzies, J. W., et al. 1989, *MNRAS*, 237, 55P, doi: [10.1093/mnras/237.1.55P](#)
- Chevalier, R. A. 1976, *ApJ*, 207, 872, doi: [10.1086/154557](#)
- Chugai, N. N. 1991, *Soviet Ast.*, 35, 171
- . 1994, *ApJL*, 428, L17, doi: [10.1086/187382](#)
- Chugai, N. N., Chevalier, R. A., Kirshner, R. P., & Challis, P. M. 1997, *ApJ*, 483, 925, doi: [10.1086/304253](#)
- Colella, P., & Glaz, H. M. 1985, *Journal of Computational Physics*, 59, 264, doi: [10.1016/0021-9991\(85\)90146-9](#)
- Colella, P., & Woodward, P. R. 1984, *Journal of Computational Physics*, 54, 174, doi: [10.1016/0021-9991\(84\)90143-8](#)
- Colgan, S. W. J., Haas, M. R., Erickson, E. F., Lord, S. D., & Hollenbach, D. J. 1994, *ApJ*, 427, 874, doi: [10.1086/174193](#)
- Crowther, P. A., Lennon, D. J., & Walborn, N. R. 2006, *A&A*, 446, 279, doi: [10.1051/0004-6361:20053685](#)
- Dessart, L., & Audit, E. 2019, *A&A*, 629, A17, doi: [10.1051/0004-6361/201935794](#)
- Dessart, L., & Hillier, D. J. 2008, *MNRAS*, 383, 57, doi: [10.1111/j.1365-2966.2007.12538.x](#)
- Dopita, M. A., Dawe, J. A., Achilleos, N., et al. 1988, *AJ*, 95, 1717, doi: [10.1086/114768](#)
- Ertl, T., Woosley, S. E., Sukhbold, T., & Janka, H. T. 2020, *ApJ*, 890, 51, doi: [10.3847/1538-4357/ab6458](#)



- France, K., McCray, R., Penton, S. V., et al. 2011, *ApJ*, 743, 186, doi: [10.1088/0004-637X/743/2/186](https://doi.org/10.1088/0004-637X/743/2/186)
- Fransson, C., Cassatella, A., Gilmozzi, R., et al. 1989, *ApJ*, 336, 429, doi: [10.1086/167022](https://doi.org/10.1086/167022)
- Fryxell, B., Arnett, D., & Müller, E. 1991, *ApJ*, 367, 619, doi: [10.1086/169657](https://doi.org/10.1086/169657)
- Gabler, M., Wongwathanarat, A., & Janka, H.-T. 2021, *MNRAS*, doi: [10.1093/mnras/stab116](https://doi.org/10.1093/mnras/stab116)
- Gear, C. W. 1971, *Numerical initial value problems in ordinary differential equations*
- Gilmozzi, R., Cassatella, A., Clavel, J., et al. 1987, *Nature*, 328, 318, doi: [10.1038/328318a0](https://doi.org/10.1038/328318a0)
- Haas, M. R., Erickson, E. F., Lord, S. D., et al. 1990, *ApJ*, 360, 257, doi: [10.1086/169115](https://doi.org/10.1086/169115)
- Hairer, E., Norsett, S. P., & Wanner, G. 1993, *Solving Ordinary Differential Equations I, Nonstiff Problems*, second revised edn. (Springer-Verlag Berlin Heidelberg), doi: [10.1007/978-3-540-78862-1](https://doi.org/10.1007/978-3-540-78862-1)
- Hairer, E., & Wanner, G. 1996, *Solving Ordinary Differential Equations II, Stiff and Differential-Algebraic Problems*, second revised edn. (Springer-Verlag Berlin Heidelberg), doi: [10.1007/978-3-642-05221-7](https://doi.org/10.1007/978-3-642-05221-7)
- Hamuy, M., Suntzeff, N. B., Gonzalez, R., & Martin, G. 1988, *AJ*, 95, 63, doi: [10.1086/114613](https://doi.org/10.1086/114613)
- Hillebrandt, W., Höflich, P., Weiss, A., & Truran, J. W. 1987, *Nature*, 327, 597, doi: [10.1038/327597a0](https://doi.org/10.1038/327597a0)
- Hillebrandt, W., & Meyer, F. 1989, *A&A*, 219, L3
- Humphreys, R. M., & McElroy, D. B. 1984, *ApJ*, 284, 565, doi: [10.1086/162439](https://doi.org/10.1086/162439)
- Jakobsen, P., Albrecht, R., Barbieri, C., et al. 1991, *ApJL*, 369, L63, doi: [10.1086/185959](https://doi.org/10.1086/185959)
- Jerkstrand, A., Smartt, S. J., Sollerman, J., et al. 2015, *MNRAS*, 448, 2482, doi: [10.1093/mnras/stv087](https://doi.org/10.1093/mnras/stv087)
- Jerkstrand, A., Wongwathanarat, A., Janka, H. T., et al. 2020, *MNRAS*, 494, 2471, doi: [10.1093/mnras/staa736](https://doi.org/10.1093/mnras/staa736)
- Kageyama, A., & Sato, T. 2004, *Geochemistry, Geophysics, Geosystems*, 5, Q09005, doi: [10.1029/2004GC000734](https://doi.org/10.1029/2004GC000734)
- Kifonidis, K., Plewa, T., Janka, H.-T., & Müller, E. 2003, *A&A*, 408, 621, doi: [10.1051/0004-6361:20030863](https://doi.org/10.1051/0004-6361:20030863)
- Kjær, K., Leibundgut, B., Fransson, C., Jerkstrand, A., & Spyromilio, J. 2010, *A&A*, 517, A51, doi: [10.1051/0004-6361/201014538](https://doi.org/10.1051/0004-6361/201014538)
- Kozma, C., & Fransson, C. 1998, *ApJ*, 497, 431, doi: [10.1086/305452](https://doi.org/10.1086/305452)
- Kunkel, W., Madore, B., Shelton, I., et al. 1987, *IAUC*, 4316
- Langer, N. 1991, *A&A*, 243, 155
- Larsson, J., Fransson, C., Kjaer, K., et al. 2013, *ApJ*, 768, 89, doi: [10.1088/0004-637X/768/1/89](https://doi.org/10.1088/0004-637X/768/1/89)
- Larsson, J., Fransson, C., Spyromilio, J., et al. 2016, *ApJ*, 833, 147, doi: [10.3847/1538-4357/833/2/147](https://doi.org/10.3847/1538-4357/833/2/147)
- Larsson, J., Spyromilio, J., Fransson, C., et al. 2019, *ApJ*, 873, 15, doi: [10.3847/1538-4357/ab03d1](https://doi.org/10.3847/1538-4357/ab03d1)
- Li, H., & McCray, R. 1992, *ApJ*, 387, 309, doi: [10.1086/171082](https://doi.org/10.1086/171082)
- Liou, M.-S. 1996, *Journal of Computational Physics*, 129, 364, doi: [10.1006/jcph.1996.0256](https://doi.org/10.1006/jcph.1996.0256)
- Lundqvist, P., & Fransson, C. 1996, *ApJ*, 464, 924, doi: [10.1086/177380](https://doi.org/10.1086/177380)
- Maguire, K., Jerkstrand, A., Smartt, S. J., et al. 2012, *MNRAS*, 420, 3451, doi: [10.1111/j.1365-2966.2011.20276.x](https://doi.org/10.1111/j.1365-2966.2011.20276.x)
- Mazzali, P. A., Lucy, L. B., & Butler, K. 1992, *A&A*, 258, 399
- McCray, R. 1993, *ARA&A*, 31, 175, doi: [10.1146/annurev.aa.31.090193.001135](https://doi.org/10.1146/annurev.aa.31.090193.001135)
- Menon, A., & Heger, A. 2017, *MNRAS*, 469, 4649, <https://arxiv.org/abs/1703.04918>
- Menon, A., Utrobin, V., & Heger, A. 2019, *MNRAS*, 482, 438, doi: [10.1093/mnras/sty2647](https://doi.org/10.1093/mnras/sty2647)
- Mihalas, D., & Mihalas, B. W. 1984, *Foundations of radiation hydrodynamics*
- Morris, T., & Podsiadlowski, P. 2009, *MNRAS*, 399, 515, doi: [10.1111/j.1365-2966.2009.15114.x](https://doi.org/10.1111/j.1365-2966.2009.15114.x)
- Müller, E., Fryxell, B., & Arnett, D. 1991a, in *European Southern Observatory Conference and Workshop Proceedings*, Vol. 37, *European Southern Observatory Conference and Workshop Proceedings*, ed. I. J. Danziger & K. Kjaer, 99
- Müller, E., Fryxell, B., & Arnett, D. 1991b, *A&A*, 251, 505
- Müller, E., & Steinmetz, M. 1995, *Computer Physics Communications*, 89, 45, doi: [10.1016/0010-4655\(94\)00185-5](https://doi.org/10.1016/0010-4655(94)00185-5)
- Nomoto, K., & Hashimoto, M. 1988, *PhR*, 163, 13, doi: [10.1016/0370-1573\(88\)90032-4](https://doi.org/10.1016/0370-1573(88)90032-4)
- Ono, M., Nagataki, S., Ferrand, G., et al. 2020, *ApJ*, 888, 111, doi: [10.3847/1538-4357/ab5dba](https://doi.org/10.3847/1538-4357/ab5dba)
- Phillips, M. M., Heathcote, S. R., Hamuy, M., & Navarrete, M. 1988, *AJ*, 95, 1087, doi: [10.1086/114705](https://doi.org/10.1086/114705)
- Podsiadlowski, P. 1992, *PASP*, 104, 717, doi: [10.1086/133043](https://doi.org/10.1086/133043)
- Podsiadlowski, P., & Joss, P. C. 1989, *Nature*, 338, 401, doi: [10.1038/338401a0](https://doi.org/10.1038/338401a0)
- Podsiadlowski, P., Joss, P. C., & Hsu, J. J. L. 1992, *ApJ*, 391, 246, doi: [10.1086/171341](https://doi.org/10.1086/171341)
- Podsiadlowski, P., Joss, P. C., & Rappaport, S. 1990, *A&A*, 227, L9
- Podsiadlowski, P., Morris, T. S., & Ivanova, N. 2007, in *American Institute of Physics Conference Series*, Vol. 937, *Supernova 1987A: 20 Years After: Supernovae and Gamma-Ray Bursters*, ed. S. Immler, K. Weiler, & R. McCray, 125–133, doi: [10.1063/1.3682893](https://doi.org/10.1063/1.3682893)
- Quirk, J. J. 1994, *International Journal for Numerical Methods in Fluids*, 18, 555, doi: [10.1002/fld.1650180603](https://doi.org/10.1002/fld.1650180603)
- Rousseau, J., Martin, N., Prévot, L., et al. 1978, *A&AS*, 31, 243
- Saio, H., Nomoto, K., & Kato, M. 1988, *Nature*, 334, 508, doi: [10.1038/334508a0](https://doi.org/10.1038/334508a0)

- Scheck, L., Kifonidis, K., Janka, H.-T., & Müller, E. 2006, *A&A*, 457, 963, doi: [10.1051/0004-6361:20064855](https://doi.org/10.1051/0004-6361:20064855)
- Searle, S. C., Prinja, R. K., Massa, D., & Ryans, R. 2008, *A&A*, 481, 777, doi: [10.1051/0004-6361:20077125](https://doi.org/10.1051/0004-6361:20077125)
- Sedov, L. I. 1959, *Similarity and Dimensional Methods in Mechanics*
- Seitenzahl, I. R., Timmes, F. X., & Magkotsios, G. 2014, *ApJ*, 792, 10, doi: [10.1088/0004-637X/792/1/10](https://doi.org/10.1088/0004-637X/792/1/10)
- Shigeyama, T., & Nomoto, K. 1990, *ApJ*, 360, 242, doi: [10.1086/169114](https://doi.org/10.1086/169114)
- Sonneborn, G., Altner, B., & Kirshner, R. P. 1987, *ApJL*, 323, L35, doi: [10.1086/185052](https://doi.org/10.1086/185052)
- Sukhbold, T., Ertl, T., Woosley, S. E., Brown, J. M., & Janka, H.-T. 2016, *ApJ*, 821, 38, doi: [10.3847/0004-637X/821/1/38](https://doi.org/10.3847/0004-637X/821/1/38)
- Suntzeff, N. B., & Bouchet, P. 1990, *AJ*, 99, 650, doi: [10.1086/115358](https://doi.org/10.1086/115358)
- Suntzeff, N. B., Hamuy, M., Martin, G., Gomez, A., & Gonzalez, R. 1988, *AJ*, 96, 1864, doi: [10.1086/114933](https://doi.org/10.1086/114933)
- Trundle, C., Lennon, D. J., Puls, J., & Dufton, P. L. 2004, *A&A*, 417, 217, doi: [10.1051/0004-6361:20034325](https://doi.org/10.1051/0004-6361:20034325)
- Truran, J. W., & Weiss, A. 1987, in *Lecture Notes in Physics*, Berlin Springer Verlag, Vol. 287, Nuclear Astrophysics, ed. W. Hillebrandt, R. Kuhfuss, E. Mueller, & J. W. Truran, 293–304, doi: [10.1007/BFb0016590](https://doi.org/10.1007/BFb0016590)
- Urushibata, T., Takahashi, K., Umeda, H., & Yoshida, T. 2018, *MNRAS*, 473, L101, doi: [10.1093/mnras/slx166](https://doi.org/10.1093/mnras/slx166)
- Utrobin, V. P. 2004, *Astronomy Letters*, 30, 293, doi: [10.1134/1.1738152](https://doi.org/10.1134/1.1738152)
- . 2005, *Astronomy Letters*, 31, 806, doi: [10.1134/1.2138767](https://doi.org/10.1134/1.2138767)
- . 2007, *A&A*, 461, 233, doi: [10.1051/0004-6361:20066078](https://doi.org/10.1051/0004-6361:20066078)
- Utrobin, V. P., & Chugai, N. N. 2005, *A&A*, 441, 271, doi: [10.1051/0004-6361:20042599](https://doi.org/10.1051/0004-6361:20042599)
- Utrobin, V. P., Chugai, N. N., & Andronova, A. A. 1995, *A&A*, 295, 129
- Utrobin, V. P., Wongwathanarat, A., Janka, H.-T., & Müller, E. 2015, *A&A*, 581, A40, doi: [10.1051/0004-6361/201425513](https://doi.org/10.1051/0004-6361/201425513)
- Utrobin, V. P., Wongwathanarat, A., Janka, H.-T., et al. 2019, *A&A*, 624, A116, doi: [10.1051/0004-6361/201834976](https://doi.org/10.1051/0004-6361/201834976)
- Walborn, N. R., Lasker, B. M., Laidler, V. G., & Chu, Y.-H. 1987, *ApJL*, 321, L41, doi: [10.1086/185002](https://doi.org/10.1086/185002)
- Wampler, E. J., Wang, L., Baade, D., et al. 1990, *ApJL*, 362, L13, doi: [10.1086/185836](https://doi.org/10.1086/185836)
- Weiss, A. 1989, *ApJ*, 339, 365, doi: [10.1086/167302](https://doi.org/10.1086/167302)
- Weiss, A., Hillebrandt, W., & Truran, J. W. 1988, *A&A*, 197, L11
- West, R. M., Lauberts, A., Jorgensen, H. E., & Schuster, H. E. 1987, *A&A*, 177, L1
- Wongwathanarat, A., Hammer, N. J., & Müller, E. 2010, *A&A*, 514, A48, doi: [10.1051/0004-6361/200913435](https://doi.org/10.1051/0004-6361/200913435)
- Wongwathanarat, A., Janka, H.-T., & Müller, E. 2013, *A&A*, 552, A126, doi: [10.1051/0004-6361/201220636](https://doi.org/10.1051/0004-6361/201220636)
- Wongwathanarat, A., Janka, H.-T., Müller, E., Pllumbi, E., & Wanajo, S. 2017, *ApJ*, 842, 13, doi: [10.3847/1538-4357/aa72de](https://doi.org/10.3847/1538-4357/aa72de)
- Wongwathanarat, A., Müller, E., & Janka, H.-T. 2015, *A&A*, 577, A48, doi: [10.1051/0004-6361/201425025](https://doi.org/10.1051/0004-6361/201425025)
- Woosley, S. E., Heger, A., Weaver, T. A., & Langer, N. 1997
- Woosley, S. E., Pinto, P. A., & Ensman, L. 1988, *ApJ*, 324, 466, doi: [10.1086/165908](https://doi.org/10.1086/165908)